Validation of Electromagnetic CAD Human Phantoms

by

Harshal Tankaria

A Dissertation

Submitted to the Faculty

of the

WORCESTER POLYTECHNIC INSTITUTE

in partial fulfillment of the requirements for the

Master of Science

In

Electrical and Computer Engineering

April 2017

APPROVED:

Dr. Sergey Makarov _____
Worcester Polytechnic Institute

Dr. Gregory Noetscher _____

US Army Natick Soldier Research, Development, and Engineering Center

Dr. Janakinadh Yanamadala _____

MathWorks, Inc.

To my parents

Abstract

About fifty years ago, research began in the field of computational human phantoms primarily for radiation dose calculations. This field has grown exponentially due to the potential for solving complicated medical problems. Modeling electromagnetic, structural, thermal, and acoustic response of the human body to different internal and external stimuli has been limited by the availability of numerically efficient computational human models.

This study describes the recent development of a computational full-body human phantom –Visible Human Project (VHP)–Female Model. This human phantom has been validated for certain frequencies in the ISM band and beyond. The anatomical accuracy of the phantom is established by comparing the CAD phantom with the original VHP image dataset.

This thesis also applies the VHP – Female CAD Model (*version 3.1*) for investigating the effects of MRI radiation. The simulation environment ANSYS HFSS is used for studying the effects of RF birdcage coil on the human phantom. Finally, a non-ionizing technique for osteoporosis detection is investigated numerically.

Acknowledgement

First and foremost, I would like to express my sincere gratitude to Professor Sergey Makarov for his continuous advice, guidance and encouragement. He motivated me and brought the best out of me. He is an inspiration and always been the key to my success. I am fortunate to have an advisor of such immense knowledge and patience. His commitment to students and work will be a benchmark for the rest of my career.

I sincerely thank Dr. Gene Bogdanov for sharing his knowledge and guidance. Dr. Gregory Noetscher of US Army Natick Soldier Research, Development, and Engineering Center, Dr. Janakinadh Yanamadala of The Mathworks for their insightful comments and constructive criticism. William Appleyard for his support and building excellent experimental set-up.

I would also like to thank my fellow team members Anh Le Tran, Aung Thu Htet, Edward Burnham, Mariya Zagalskaya, Patrick Carberry, and Patrick Lacroix, for their valuable thoughts and contributions. Best of luck to you all!

I express thanks to my grandparents, Bansilal Tankaria and Jayshree Tankaria for their blessings. My parents, Vipul Tankaria and Bina Tankaria who have been inspiring and supportive throughout this journey, I am ever grateful for their support.

Table of Contents

List of Figures

List of Tables

List of Published and Accepted Papers

1. S. N. Makarov, W. Appleyard, P. D. Carberry, **H. Tankaria**, G. M. Noetscher, "Novel On-Body Microwave Antenna Array Testbed for Highly- Sensitive Measurement of Wrist Bone Signature", *IEEE International Symposium on Antennas and Propagation and USNC-URSI Radio Science Meeting*, San Diego, 2017

2. M. Kozlov, **H. Tankaria,** G. M. Noetscher, S. N. Makarov, "Comparative Analysis of Different Versions of a Human Model Located inside a 1.5T MRI Whole Body RF Coil", *39th Annual International Conference of the IEEE Engineering in Medicine and Biology Society (EMBC), South Korea, 2017*

3. A. L. Tran, S. N. Makarov, **H. Tankaria,** "Degree of RF MRI coil Detuning and SAR Variations over an Anatomically Realistic Respiratory Cycle Modeled with the Finite Element Method*", 25th International Society for Magnetic Resonance in Medicine , Hawaii, 2017*

4. **H. Tankaria**, X. J. Jackson, R. Borwankar, G. K. Srichandru, A. L. Tran, J. Yanamadala, G. M. Noetscher, A. Nazarian, S. Louie, S. N. Makarov, "VHP-Female Full-Body Human CAD Model for Cross-Platform FEM Simulations – Recent Development and Validations*", 38th Annual International Conference of the IEEE Engineering in Medicine and Biology Society (EMBC)*,pp. 2232-2235 Florida, August 2016

5. G. M. Noetscher, J. Yanamadala, **H. Tankaria**, S. Louie, A. Prokop, A. Nazarian, and S. N. Makarov, "Computational Human Model VHP-Female Derived from Datasets of National Library of Medicine", 38th Annual International Conference of the IEEE Engineering in Medicine and Biology Society (EMBC), pp. 3350-3353, Florida, August 2016

6. J. Yanamadala, R. Borwankar, G. K. Srichandhru, A. L. Tran, **H. Tankaria**, S. N. Makarov, "Full- Body FEM Computational Pregnant Woman Model and Applications", *38th Annual International Conference of the IEEE Engineering in Medicine and Biology Society (EMBC)*, Florida, August 2016

7. A. L. Tran, R. Borwankar, **H. Tankaria**, G. K. Srichandhru, J. Yanamadala, S. Louie, S. N. Makarov, "Construction of Approximate Breathing Sequence for a CAD Human Model via a Native Parametric Sweep in ANSYS", *38th Annual International Conference of the IEEE Engineering in Medicine and Biology Society (EMBC)*, Florida, August 2016

Chapter 1
Introduction and Basic Review of Computational Human modeling in the Electromagnetic domain.

Motivation for computational human modeling

About fifty years ago, research began in the field of computational human phantoms primarily for radiation dose calculations [1]. This field has grown exponentially due to the potential for solving complicated medical problems. These phantoms have served as a great tool for studying the effects of ionizing as well as non-ionizing radiations on soft tissues and bones. Research on computational human phantom has a direct impact on the health physicist, who often needs to understand how radiation interacts with the human body so they can ensure the safety of the human workers as well as set regulatory standards.

The human body is exposed to ionizing [2] radiation during the imaging process for nuclear medicine. This involves the powerful x-ray and gamma-ray photons traversing the bodily tissues. These radiation doses need optimization which enables us to obtain high quality images while avoiding harmful radiobiological effects.

At this point in time, computational human phantoms with state-of-the-art anatomical accuracy have been developed. This presents a great opportunity to investigate and validate the human phantom for certain frequencies in the ISM band [1] and beyond. This study assists health practitioners as well as engineers and researchers in gaining a deeper perspective for testing various high frequency medical procedures on the human phantom. This enables the safety of the patient and plays a significant role in establishing and improving standards.

1.1 Review of the Visible Human Project® (VHP) dataset

1.1.1 Project concept

The Visible Human Project® (VHP) [3] is an outgrowth of the National Library of Medicine's 1986 long-range plan. One of the goals of the VHP is to construct body tissues from the anatomical images [4]. The significance of this project is to enable advanced medical research.

In 1989, the National Library of Medicine (NLM) established the VHP with a purpose to build a digital library of volumetric data representing an adult male and female anatomy. Along with the image data, software packages were also released to visualize the anatomy which was constructed from the volumetric image data.

Insight Toolkit (ITK) is an open source public software by a collaboration of six principle organizations. The tool enables segmentation and classification of tissues from the anatomical images of the VHP. Since the development of CAD human phantoms finds its roots in the dataset of images, the details are of utmost importance as discussed in the following section.

1.1.2 The dataset of images

In November 1994, the male dataset was made available by NLM. This digital library consisted of Magnetic Resonance Imaging (MRI), X-ray Computed Tomography (CT), and cryosection images.

Figure 1.1 Cryosection image (Thorax) from the original dataset (VHP-Female) of images provided by U.S. National Library of Medicine

Figure 1.2 Cryosection image (Head) from the original dataset (VHP-Female) of images provided by U.S. National Library of Medicine

1.1.3 List of major full-body models

TABLE1.1: MAJOR ANATOMICAL FULL-BODY HUMAN MODELS FOR COMPUTATION ELECTROMAGNETIC AND RADIOLOGICAL SIMULATIONS [2]

Model	Height [m]	Weight [kg]	Race	Age	Sex	Data Format, voxel resolution	Comment	Available from
Child	1.15	21.7	Caucasian	7 y	F	1.54x1.54x8mm^3	Small for age	www.cst.com www.ascension.de
Baby	0.57	4.2	Caucasian	8 w	F	0.85x0.85x4mm^3		www.cst.com www.ascension.de
VoxelMan			Caucasian	adult	M		Head and torso	
Norman			Caucasian	adult	M		only 10 ribs	
Golem	1.76	68.9	Caucasian	38 y	M	2.08x2.08x8mm^3		www.cst.com www.ascension.de
Visible-human			Caucasian	38 y	M	various	One testicle only	www.speag.com www.remcom.com
Frank	1.74	95	Caucasian	48 y	M	0.74x0.74x5mm^3	head and torso	
Donna	1.70	79	Caucasian	40 y	F	1.875x1.875x10mm^3		www.cst.com www.ascension.de
Helga	1.70	81	Caucasian	26 y	F	0.98x0.98x10mm^3		www.cst.com www.ascension.de
Irene	1.63	51	Caucasian	32 y	F	1.875x1.875x5mm^3		
Max			Caucasian	adult	M		VoxelMan adapted to dimensions of reference man	
Nagaoka man			Asian	22 years	M	2x2x2mm^3		
Nagaoka woman			Asian	22 years	F	2x2x2mm^3		
Naomi			Caucasian	23-year-old	F			
Katja	1.63	62.3	Caucasian	43 years	F	1.775x1.775x4.8mm^3	Pregnant (24th week)	www.cst.com www.ascension.de
Roberta	1.08	17.6	Caucasian	5 years	F	CAD, 0.5x0.5x0.5mm^3 or better		www.itis.ethz.ch
Thelonious	1.17	19.5	Caucasian	6 years	M	CAD, 0.5x0.5x0.5mm^3 or better		www.itis.ethz.ch

Model	Height [m]	Weight [kg]	Race	Age	Sex	Data Format, voxel resolution	Comment	Available from
Eartha	1.35	30.3	Caucasian	8 years	F	CAD, 0.5x0.5x0.5mm^3 or better		www.itis.ethz.ch
Dizzie	1.40	26.2	Caucasian	8 years	M	CAD, 0.5x0.5x0.5mm^3 or better		www.itis.ethz.ch
Billie	1.46	35.6	Caucasian	11 years	F	CAD, 0.5x0.5x0.5mm^3 or better		www.itis.ethz.ch
Louis	1.69	49.9	Caucasian	14 years	M	CAD, 0.5x0.5x0.5mm^3 or better		www.itis.ethz.ch
Ella	1.60	58	Caucasian	26 years	F	CAD, 0.5x0.5x0.5mm^3 or better		www.itis.ethz.ch
Duke	1.74	70	Caucasian	34 years	M	CAD, 0.5x0.5x0.5mm^3 or better		www.itis.ethz.ch www.virtualman.info
Ella (pregnant)	1.60		Caucasian	26 years	F	CAD	3rd, 7th and 9th gestational month	www.speag.com
Fats	1.78	120	Caucasian	37 years	M	CAD		www.speag.com
Chinese Male	1.72	63.05	Asian	35 years	M	1x1x1mm^3		
Chinese Female	1.62	53.5	Asian	22 years	F	1x1x1mm^3		
VHP-F	1.73	~ 75	Caucasian	~ 60 yrs	F	Variable. Average: 2x2x2 mm^3	Visible Human Data Source. Variable Fat Layer	www.nevaelectromagnetics.com

1.2 Overview of the numerical simulation environment.

1.2.1 Commercial Electromagnetic packages

To study the effects of radiation on the human phantom, it is required to select the appropriate solver and solution method. The end goal is to solve the Maxwell equations and obtain the solution for the Electric and Magnetic fields.

The full wave solvers are categorized on the basis of their solution method [5]: Integral Equations (IE) solved by Method of Moments (MoM), Finite Elements (FE), Finite-Differences Time-Domain (FDTD), and Finite Integration Technique (FIT). A history and a comprehensive overview of the different numerical techniques and of their application in Computational Electromagnetics (CEM) may be found in [6]. Recent work on the latest developments in CEM [7] concentrates on the two main approaches of differential and integral methods. A good review and perspectives concerning the relationship between differential and integral equations (IE) modeling is recommended in a review paper by Miller [8]. A thorough discussion on the different techniques with clarifying examples is also given in [9].

Having studied various packages and solution methods, the focus has been on the ANSYS simulation environment due to the solution method and workflow of this package. The following section discusses the ANSYS environment as well as the Finite Element Method.

1.2.2 Simulation set-up (ANSYS HFSS)

The Finite Element Method (FEM) [10], [11] is a method based on solving partial differential equations. It is most commonly formulated based on a variational expression. It subdivides space in elements, for example tetrahedra. Fields inside these elements are expressed in terms of a number of basic functions, for example polynomials. These expressions are inserted into the functions of the equations, and the variation of the functional is made zero. This yields a matrix eigenvalue equation whose solution yields the fields at the nodes.

Its first formulations were developed as matrix methods for structural mechanics. This lead to the idea to approximate solids and Courant (1942) introduced an assembly of triangular elements and the minimum of potential energy to torsion problems [12]. The first paper on the application of FEM to electrical problems appeared in 1968 [13]. An extensive review on the history of FEM in electromagnetics was published in an issue of the Antennas and Propagation Magazine [14]. FEM normally is formulated in the frequency domain, i.e. for time-harmonic problems. This means that, as for IE-MoM, the solution has to be calculated for every frequency of interest. Numerous references can be given developing, explaining, and using FEM, including the seminal text given in [11]. A software tool using FEM and very widely spread is ANSYS HFSS.

ANSYS HFSS (High Frequency Structural Simulation)

The adaptive solution process enables HFSS to guarantee the accuracy of the final answer for a given EM problem. The process [15] is described below:

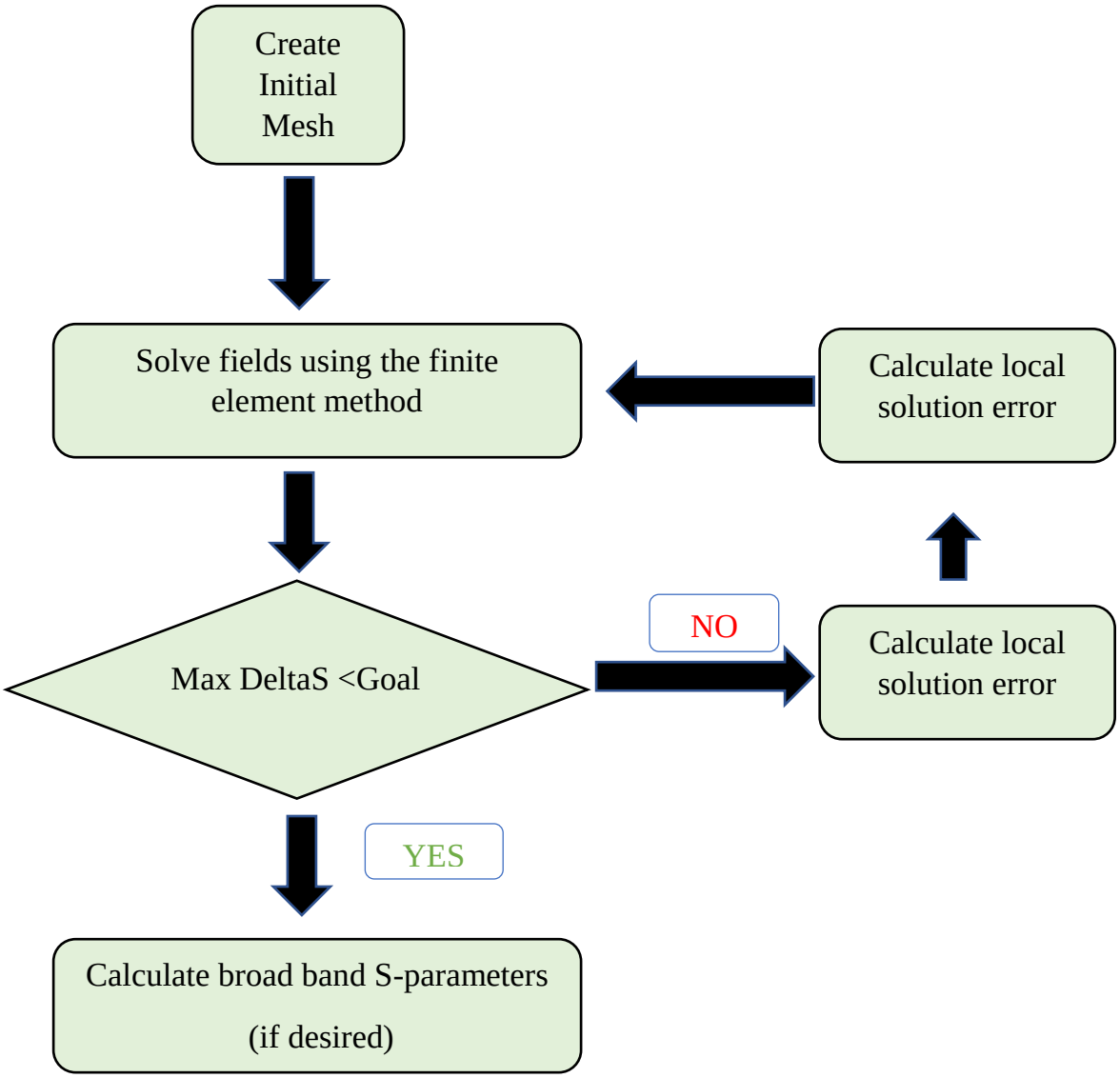

Figure 1.3 The adaptive solution process for accurate simulation results

1.2.3 Mesh healing packages (ANSYS SpaceClaim, MeshLab)

ANSYS Spaceclaim is an extremely powerful tool, especially when working with STL files. This environment works on the ASIC kernel and runs on Windows operating system. The software architecture is written in C++. The add-on '*Facets*' toolbox is specifically designed for boolean mesh operations to create error free, manifold, and water tight meshes[18].

The tool has proven especially well-suited for visualization and healing of complicated geometry problems and has been extensively used during the development of the VHP - Female v. 3.1 model. Figure 1.4 below shows the robust skull model as seen in the SpaceClaim environment.

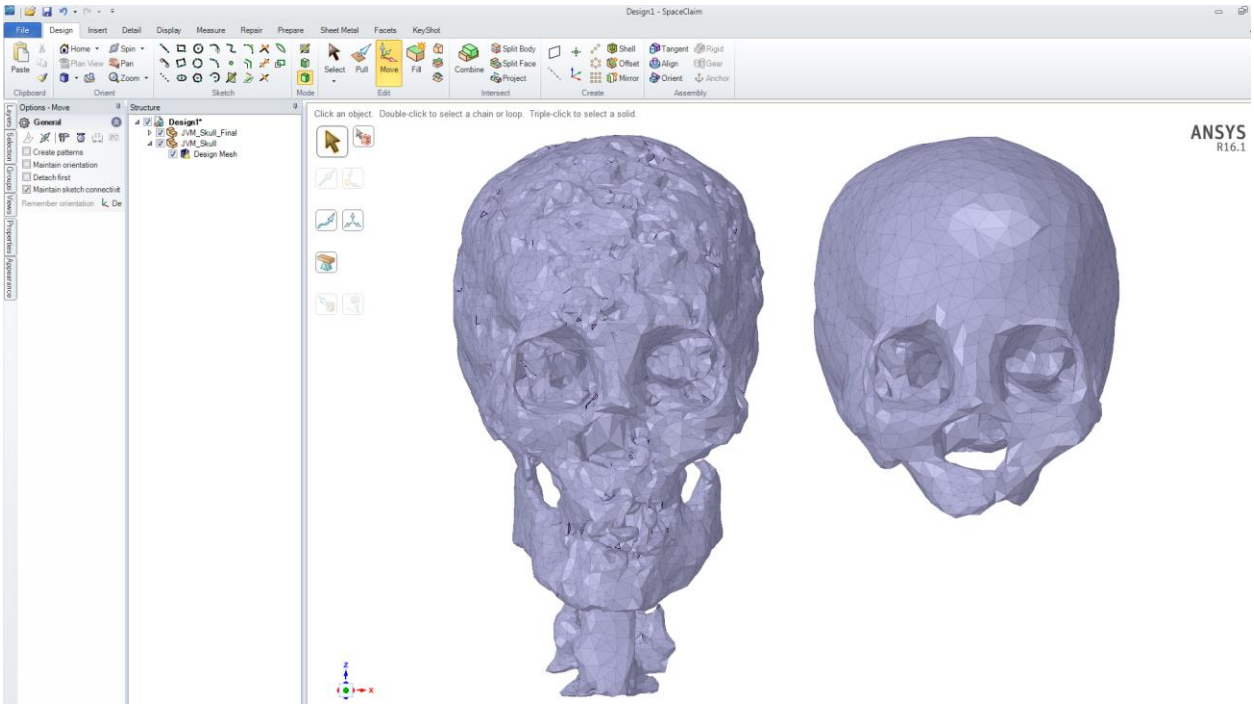

Figure 1.4 Healing the skull with bad meshes in ANSYS SpaceClaim.

MeshLab [19] is an open source tool that is useful for quick visualization as well as applying various mesh processing operations such as Laplacian smoothing. The ability to add / delete points from the mesh does not seem available at present.

1.3 Building on existing research.

Prior to my thesis VHP- Female Computational Phantoms was developed by Dr. Noetscher [16] and Dr. Yanamadala [17]. The aim for research in the topic of computational phantoms has been to achieve greater anatomical accuracy along with geometrical robustness. Chapter 2 discusses these advancements for an improved version of the VHP-Female Model.

The development of computational phantoms aids the validation of various applications and medical procedures where the phantom can be applied. A smooth, geometrically optimized model will produce accurate results as compared to rough meshes when simulated in commercial EM solver packages

1.4 Thesis organization

This thesis has been conceptualized for a deep understanding of applying the computational human phantom as a potential testbed for a wide range of application frequencies. Major work has been carried out in the RF spectrum with frequencies ranging from 64 MHz to 0.9 GHz. Chapter 2 discusses the recent developments and validations of the VHP-Female Full-Body Human CAD model. Chapter 3 primarily describes the validation of CAD human phantoms. Furthermore, a novel approach towards MRI coil tuning is explained. At this point, one of the major applications for the use of VHP-Female human phantom has been established.

This human model finds significant applications in a much broader spectrum. Chapter 4 investigates a non-ionizing technique for detection of osteoporosis. The patch antenna design along with experimental results have been presented. To conclude, this thesis stresses the importance of the computational human phantoms for the medical industry. My thesis is intended to serve researchers and medical industry professionals to investigate and test their designs and procedures for a wide frequency spectrum.

References

[1]. X. George, "An exponential growth of computational phantom research in radiation protection, imaging and radiotherapy: A review of the fifty-year history", Phys Med Biol, vol. 59, no. 8, pp. 233-302, Sept.2014.

[2]. IEEE Int. Committee on Electrmagnetic Safety: TC 34: List of human phantoms. http://grouper.ieee.org/groups/scc34/sc2/wg2/available%20human%20models.doc

[3]. https://www.nlm.nih.gov/research/visible/visible_human.html

[4]. https://www.nlm.nih.gov/research/visible/animations.html

[5]. A. E. Vandenbosch and Alexander Vasylchenk, "A Practical Guide to 3D Electromagnetic Software Tools Guy", Katholieke Universiteit ,Leuven, Belgium.

[6]. D. B. Davidson,"A review of important recent developments in full-wave CEM for RF and microwave engineering," IEEE 3rd Int. Conf. Comp. Electromagnetics and Its Applications, pp. PS/1-PS/4, Nov. 2004.

[7]. C. W. Townbridge and J. K. Sykulski,"Some Key Developments in Computational Electromagnetics and Their Attribution," IEEE Antennas and Propag. Magazine, vol. 42, no. 6, pp. 503 – 508, Apr. 2006.

[8]. E. K. Miller,"A Selective Survey of Computational Electromagnetics," IEEE Trans Antennas Propag, vol. 36, no. 9, Sept. 1988, pp. 1281 – 1305 .

[9]. F. Peterson, S. L. Ray, and R. Mittra, "Computational methods for electromagnetics", IEEE Press – Oxford University Press, 1998.

[10]. J. M. Jin, The Finite Element Method in Electromagnetics, second edition, John electromagnetics", IEEE Press – Oxford University Press, 1998.Willey & Sons, Inc., New York, 2002.

[11]. J. L. Volakis, A. Chatterjee, and L. C. Kempel, "Finite element method for electromagnetics", IEEE Press, Oxford University Press, 1997.

[12]. R. L. Courant, "Variational methods for the solution of problems of equilibrium and vibration," Bulletin of the American Mathematical Society, 5, pp. 1-23, 1943.

[13]. S. Ahmed, "Finite-element method for waveguide problems," Electronics Letters, vol. 4, Issue 18, pp.387 – 389, Sept. 1968.

[14]. R. Coccioli, T. Itoh, G. Pelosi, P. P. Silvester,"Finite-Element Methods in Microwaves: A Selected Bibliography," IEEE Antennas and Propag. Magazine, vol. 38, Issue 6, pp.34 – 48, Dec. 1996.

[15]. http://e-science.ru/sites/default/files/upload_forums_files/8u/HFSSintro.pdf

[16]. G. M. Noetscher, "The VHP-F Computational Phantom and its Applications for Electrical Simulation," Dissertation, April 2014.

[17]. J. Yanamadala, "Development of Human CAD Models and Related Mesh Processing Algorithms with Application in Bio electromagnetic" Dissertation, April 2016.

[18]. http://www.spaceclaim.com/en/Support/Tutorials/Essentials/SpaceClaim_Basics_Tutorials.aspx

[19]. P. Cignoni, M. Callieri, M. Corsini, M. Dellepiane, F. Ganovelli, G. Ranzuglia, "MeshLab: an Open-Source Mesh Processing Tool," Sixth Eurographics, Italian Chapter Conference, page 129-136, 2008.

Chapter 2

Recent developments and physical validation of the VHP-Female Full-Body Human CAD model.

2.1 INTRODUCTION

Numerical simulation of the electromagnetic and thermal response of the human body to different stimuli in MRI safety, electromagnetic tomography, and electromagnetic stimulation is currently limited by the availability of anatomically adequate and numerically efficient cross-platform computational models [1]-[5]. The first objective of this chapter is to present an improved platform-independent full-body electromagnetic computational model (computational phantom), the Visible Human Project® (VHP)-Female v. 3.1 and to describe its distinct features and enhancements compared to VHP-Female v. 2.0. The second objective is to optically validate the VHP-Female v. 3.1 with the cross sectional image dataset. This is an integral test for determining the anatomical accuracy of the phantom. In the process of discussing the development of the VHP-Female phantom, we discover the importance of certain mesh healing tools, such as ANSYS SpaceClaim, MeshLab and meshmixer. The focus is strike a balance between the preserving the anatomy and rendering a numerically efficient mesh. This development marks its importance as a full scale, anatomically true, and cross-platform compatible computational phantom which yields accurate simulation results as discussed in the following chapters.

2.2 Phantom Description

The computational phantom VHP-Female v. 3.1 shown in Fig. 2.1 includes 27 individual tissues and 248 separate tissue parts, all extracted from the open-source Visible Human Project®-Female cryosection dataset of the U.S. National Library of Medicine (NLM) [6] and in the form of 3D CAD objects (triangular surface meshes). The cryosection dataset with the resolution of 0.33 mm allowed us to visually differentiate between various soft and hard tissues.

The phantom possesses a set of topological characteristics necessary for cross-platform compatibility and computational efficiency. Each original tissue triangular surface mesh is strictly 2-manifold or thin-shell (no non-manifold faces, no non-manifold vertices, no holes, and no self-intersections). No tissue mesh has any triangular facets in contact with other tissue surfaces. There is always a (small) gap between the distinct tissue surfaces. This gap physically represents thin membranes separating distinct tissues. The surface deviation error does not generally exceed 0.5-3 mm in the head and 7 mm in the main body.

The model represents a ~60 year old white female subject with a height h of 162 cm measured from top of the scalp to the average center of both heels. The body mass M computed using standard tissue densities and assigning the average body shell, which includes internal tissues, the density of the muscle is ~88 kg. The computed BMI is ~33.5 (moderately obese). The entire phantom and the individual tissue surface meshes are available in MATLAB binary format as well as in a variety of standard CAD formats. All electromagnetic material properties are derived the IT'IS database [13].

2.3 Phantom Construction

The VHP –model has been developed from cryosection images, using various custom MATLAB tools [14]

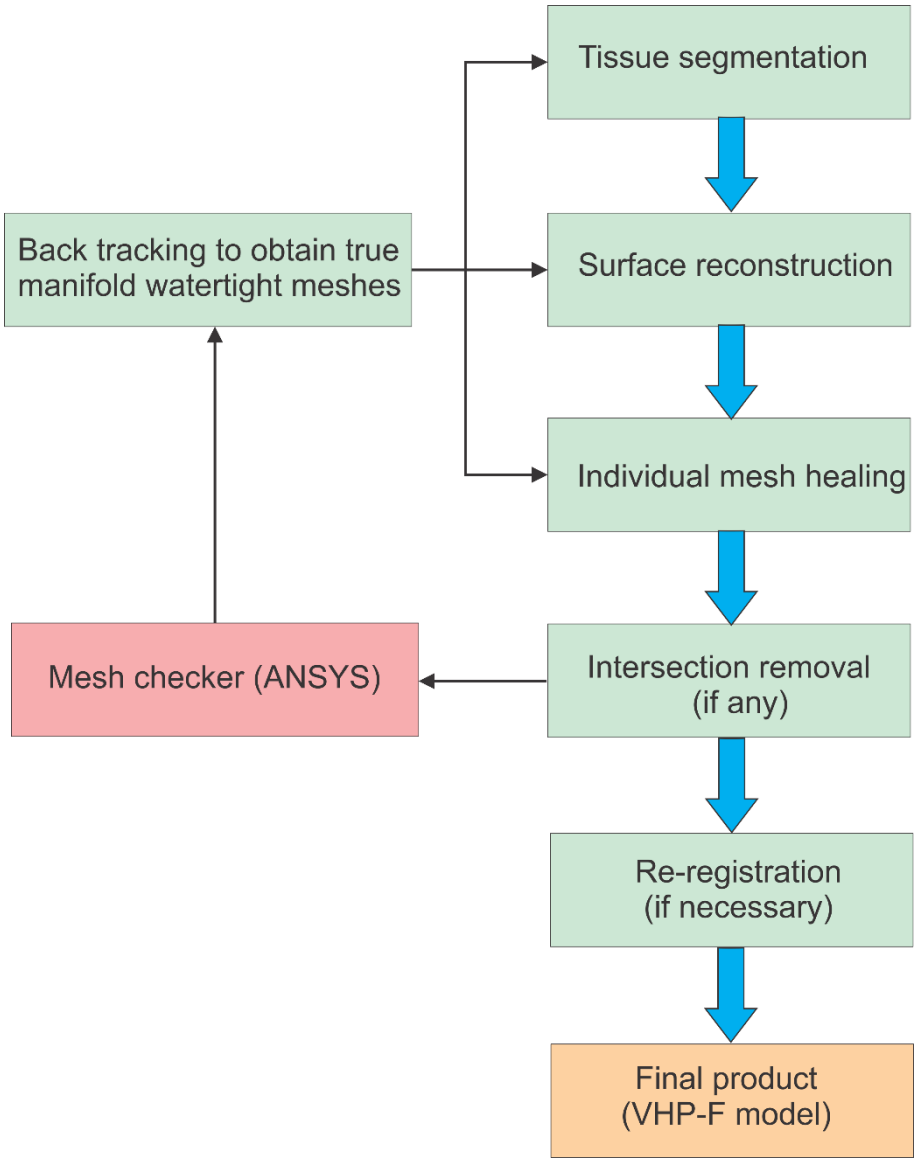

Figure. 2.1 Summary of various stages involved in the development of VHP-Female model

2.3.1 Tissue Segmentation

The anatomical images for the VHP-Female are segmented using custom MATLAB® -based tools. Segmentation is a process of extracting the points (*X, Y coordinates*) which bound a particular organ. For every image slice the points bounding a particular organ are extracted. When these points are stacked up along the Z axis, they form a three-dimensional point cloud.

A segmented image is shown in the figure below, through visual inspection, the images which contain the tissue are segmented using a custom MATLAB® -based script. Extensive use of the MATLAB® Image processing toolbox has been used in the development of this tool. More information about the custom MATLAB® tools are found in Dr. Yanamadala' s thesis [14].

In the figure below, the crosses denoted in green are the segmented points for the greymatter of the spinal cord.

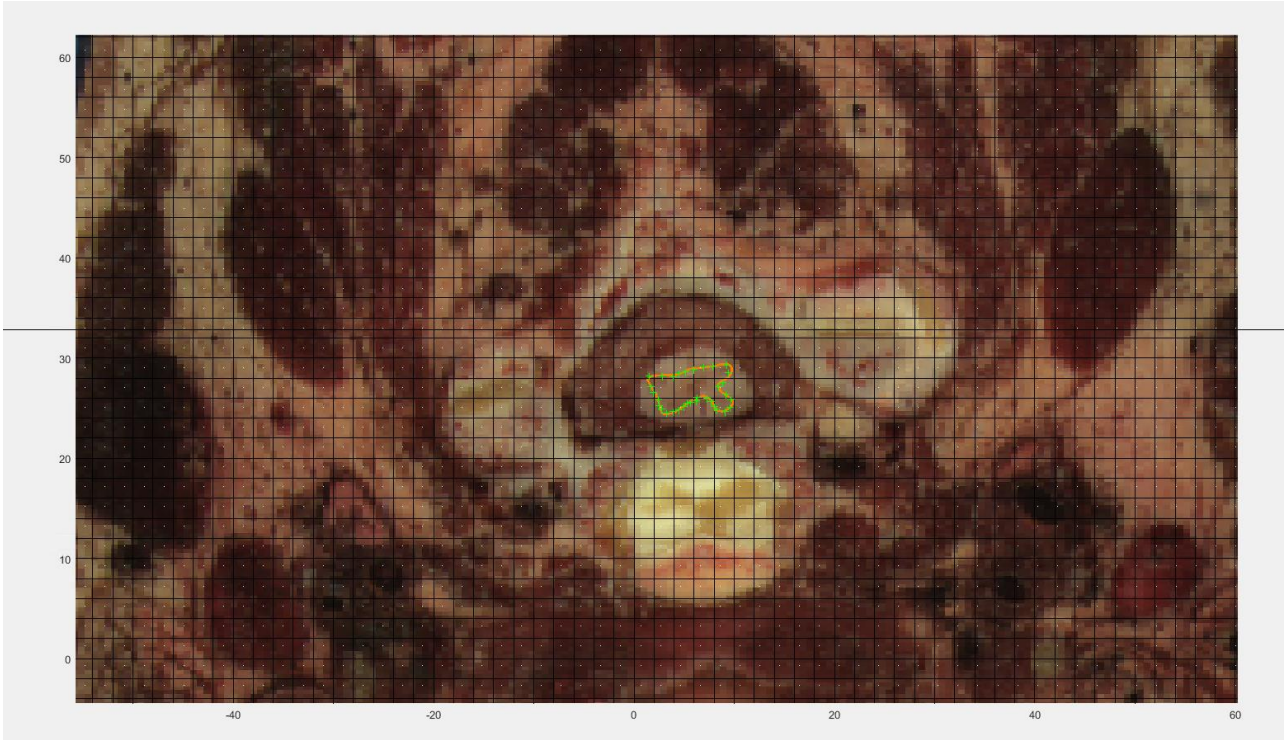

Figure. 2.2 Segmentation of an image from the VHP-Female dataset.

2.3.2 Tissue Construction

Once the tissue is segmented and we have collected all *x-y points* for every *z* slice pertaining to the tissue, a mesh constructing algorithm is used. Figure 2.3 shows the first version or the raw mesh which is generated using MyRobustCrust, an algorithm developed by Giaccari Luigi.[15]

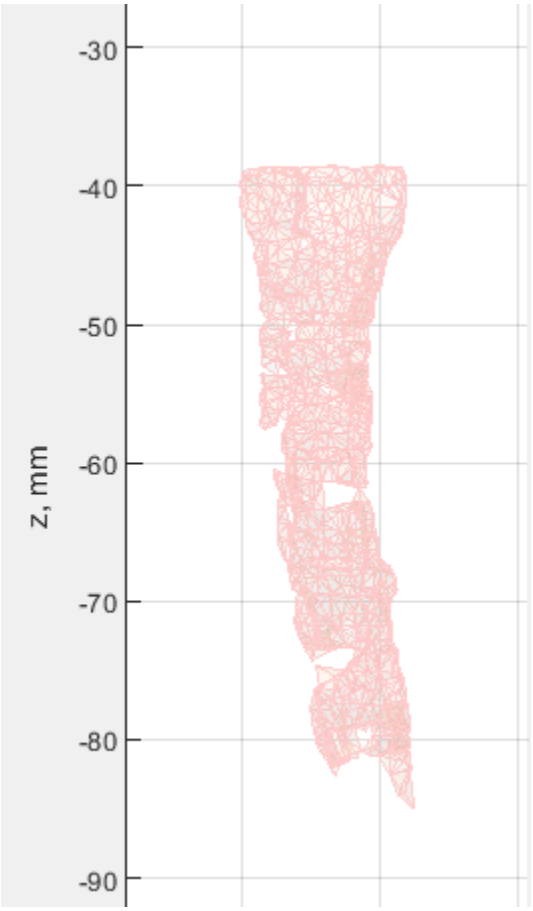

Figure 2.3 Raw version of the mesh, output of MyRobustCrust for a segment of the greymatter within the spinal cord

The above figure gives us a visual representation of the constructed mesh; this mesh is not 2-manifold and requires post processing. Mesh healing packages such as ANSYS SpaceClaim are now employed to create true CAD, manifold structures. Discussion of mesh healing packages given above in chapter 1, section 1.2.3.

2.4 Phantom Features

2.4.1 VHP –Female v. 3.1 Mesh Table

VHP Female Base Model version 3.1 March 2016

Table 2.1. List of triangular surface meshes – version 3.1

Legend:

Hard tissues	Soft tissues	Individual muscles	Cartilage	Titanium	Nervous tissues

Mesh no	Tissue name	Triangle size	Mesh quality	Min. Edge Length	Tissue Type
1	implant AMP left	498	0.004517275	0.730346488	Titanium
2	implant AMP right	498	0.004517247	0.730350564	Titanium
3	implant Femur left AMP	1068	0.011754032	0.523957408	Bone
4	implant Femur right AMP	1098	0.001032976	0.070837278	Bone
5	implant L left	2404	0.002891133	0.569885268	Titanium
6	implant L right	2448	0.002729828	0.060718349	Titanium
7	implant S left	832	0.000183283	0.028262363	Titanium
8	implant S right	836	0.000271487	0.021067037	Titanium
9	implant Trabecular lower left LI	1402	0.006146945	0.07390451	Bone
10	implant Trabecular lower right LI	1316	0.002462903	0.103316858	Bone
11	implant Trabecular upper left LI	2248	0.001040226	0.049591883	Bone
12	implant Trabecular upper left SI	1650	0.002537364	0.057516443	Bone
13	implant Trabecular upper right LI	2298	0.001212265	0.074078083	Bone
14	implant Trabecular upper right SI	1732	0.003934908	0.037323929	Bone
15	VHPC Abdominals left bot	944	0.031106169	0.597199435	Muscle
16	VHPC Abdominals left mid	762	0.040642241	0.581654081	Muscle
17	VHPC Abdominals left top	894	0.030201065	0.33161482	Muscle
18	VHPC Abdominals right bot	876	0.030734799	0.633118826	Muscle
19	VHPC Abdominals right mid	794	0.031944925	0.654299261	Muscle
20	VHPC Abdominals right top	876	0.0305205	0.304709564	Muscle
21	VHPC Arteries	10004	0.059018418	0.778119158	Blood

Mesh no	Tissue name	Triangle size	Mesh quality	Min. Edge Length	Tissue Type
22	VHPC Average Body Shell Large	8220	0.005510351	0.686529558	Average Body
23	VHPC Average Body Shell Medium	8222	0.005510373	0.686529558	Average Body
24	VHPC Average Body Shell Small	8390	0.005510378	0.686529558	Average Body
25	VHPC Bicep left	774	0.00682843	1.437837369	Muscle
26	VHPC Bicep right	792	0.092423143	0.668482594	Muscle
27	VHPC Bladder	274	0.385290549	1.65048492	Bladder
28	VHPC C01	1034	0.040807392	0.220982712	Bone
29	VHPC C02	840	0.069846699	0.225236987	Bone
30	VHPC C03	644	0.034217071	0.281392109	Bone
31	VHPC C04	740	0.05242017	0.271289302	Bone
32	VHPC C05	1258	0.047986718	0.168545793	Bone
33	VHPC C06	734	0.039014857	0.369495859	Bone
34	VHPC C07	742	0.064973386	0.525311195	Bone
35	VHPC Calcaneus left	300	0.038856421	3.309818039	Bone
36	VHPC Calcaneus right	300	0.051711435	2.742032358	Bone
37	VHPC Calf left	498	0.03996306	3.229626424	Muscle
38	VHPC Calf right	492	0.040220608	2.61529154	Muscle
39	VHPC Cerebellum	504	0.031718617	1.30500173	Cerebellum
40	VHPC Clavicle left	404	0.016117309	0.158714873	Bone
41	VHPC Clavicle right	198	0.038300057	0.353300599	Bone
42	VHPC Coccyx	150	0.082590886	1.605248503	Bone
43	VHPC CSF Extra Shell	2942	0.237841551	2.402087407	Cerebro-spinal Fluid
44	VHPC CSF Outer Shell Head Spinal Cord	4054	0.087116151	0.994720976	Cerebro-spinal Fluid
45	VHPC CSF Ventricles	630	0.037171286	0.748328597	Cerebro-spinal Fluid
46	VHPC Cuboid Left	246	0.062401287	1.885494055	Bone
47	VHPC Cuboid Right	250	0.075728253	1.613976286	Bone
48	VHPC Cuneiform Intermediate Left	148	0.054935812	1.779781475	Bone
49	VHPC Cuneiform Intermediate Right	148	0.059645276	1.43307175	Bone
50	VHPC Cuneiform Lateral Left	200	0.102289825	1.980674188	Bone
51	VHPC Cuneiform Lateral Right	150	0.033253103	2.194397072	Bone

Mesh no	Tissue name	Triangle size	Mesh quality	Min. Edge Length	Tissue Type
52	VHPC Cuneiform Medial Left	150	0.042568565	1.989996766	Bone
53	VHPC Cuneiform Medial Right	250	0.035573844	1.625215997	Bone
54	VHPC Deltoid Left	580	0.049147569	1.732133832	Muscle
55	VHPC Deltoid Right	582	0.030405681	0.935826378	Muscle
56	VHPC discC02C03	148	0.272018981	0.913219325	Cartilage
57	VHPC discC03C04	138	0.260892911	0.92314782	Cartilage
58	VHPC discC04C05	290	0.051378318	0.211030989	Cartilage
59	VHPC discC05C06	144	0.28947529	0.933645405	Cartilage
60	VHPC discC06C07	142	0.107635322	1.180624006	Cartilage
61	VHPC discC07T01	148	0.169035212	0.805997737	Cartilage
62	VHPC discL01L02	152	0.085630709	1.689779095	Cartilage
63	VHPC discL02L03	144	0.194080171	2.05669893	Cartilage
64	VHPC discL03L04	142	0.134193921	1.640631607	Cartilage
65	VHPC discL04L05	142	0.073761063	1.495614494	Cartilage
66	VHPC discL05L06	148	0.056763523	1.558606115	Cartilage
67	VHPC discL06S00	218	0.08906068	1.692565718	Cartilage
68	VHPC discT01T02	138	0.171542258	0.910752649	Cartilage
69	VHPC discT02T03	144	0.128713406	0.784934177	Cartilage
70	VHPC discT03T04	166	0.101602075	0.735298321	Cartilage
71	VHPC discT04T05	164	0.085921211	0.843557623	Cartilage
72	VHPC discT05T06	154	0.109265565	0.647093445	Cartilage
73	VHPC discT06T07	152	0.035533664	0.320949415	Cartilage
74	VHPC discT07T08	150	0.086839685	0.474222314	Cartilage
75	VHPC discT08T09	180	0.057829071	0.660032291	Cartilage
76	VHPC discT09T10	146	0.160315984	1.214273422	Cartilage
77	VHPC discT10T11	174	0.083161447	0.873448922	Cartilage
78	VHPC discT11T12	148	0.057611674	1.165868858	Cartilage
79	VHPC discT12L01	132	0.053827967	1.003560865	Cartilage
80	VHPC Erector spinae left	1138	0.059312261	2.55100727	Nerves
81	VHPC Erector spinae right	1130	0.021594585	1.465558942	Nerves
82	VHPC Eye left	100	0.16811944	3.024552146	Eye (Vitrous Humor)
83	VHPC Eye right	100	0.083365557	2.376452083	Eye (Vitrous Humor)
84	VHPC Fat Shell	8160	0.023196741	1.055549564	Fat (Average Infiltrated)
85	VHPC Feet1Phalange left	402	0.032678854	0.259928379	Bone

Mesh no	Tissue name	Triangle size	Mesh quality	Min. Edge Length	Tissue Type
86	VHPC Feet1Phalange right	200	0.079174287	1.758535341	Bone
87	VHPC Feet2Phalange left	200	0.070228587	1.621960343	Bone
88	VHPC Feet2Phalange right	300	0.06139816	0.785928615	Bone
89	VHPC Feet3Phalange left	300	0.06424283	0.679634924	Bone
90	VHPC Feet3Phalange right	250	0.049499469	1.710496646	Bone
91	VHPC Feet4Phalange left	300	0.048051362	1.031071812	Bone
92	VHPC Feet4Phalange right	250	0.045377085	1.617203323	Bone
93	VHPC Feet5Phalange left	200	0.06428668	1.727351614	Bone
94	VHPC Feet5Phalange right	200	0.071864975	1.654206141	Bone
95	VHPC Femur Bone Marrow Left	1172	0.000661496	0.258666253	Bone Marrow
96	VHPC Femur Bone Marrow Right	306	0.032371369	1.33740442	Bone Marrow
97	VHPC Femur left	996	0.047503099	3.156869759	Bone
98	VHPC Femur right	998	0.05439824	2.900155321	Bone
99	VHPC Fibula left	716	0.050388328	1.846849841	Bone
100	VHPC Fibula right	700	0.040315704	1.204957101	Bone
101	VHPC Forearm Flexors left	978	0.1170271	1.691993472	Muscle
102	VHPC Forearm Flexors right	848	0.09240119	1.547269996	Muscle
103	VHPC Gluteus left	492	0.051288985	3.787034391	Muscle
104	VHPC Gluteus right	538	0.03625148	4.527551304	Muscle
105	VHPC GreyMatter	2942	0.148597549	2.14003131	Brain (Grey Matter)
106	VHPC Hamstring left	994	0.03109203	2.715810459	Muscle
107	VHPC Hamstring right	592	0.03032495	2.634483588	Muscle
108	VHPC Hands1Phalange left	150	0.075709573	1.254111154	Bone
109	VHPC Hands1Phalange right	200	0.034203623	1.672890502	Bone
110	VHPC Hands2Phalange left	220	0.035918861	2.780488463	Bone
111	VHPC Hands2Phalange right	220	0.086287759	2.234519185	Bone
112	VHPC Hands3Phalange left	228	0.116624174	2.295026484	Bone
113	VHPC Hands3Phalange right	220	0.030221953	2.053577327	Bone
114	VHPC Hands4Phalange left	220	0.175395367	1.526234206	Bone
115	VHPC Hands4Phalange right	220	0.046221901	0.592715498	Bone
116	VHPC Hands5Phalange left	220	0.07264328	2.06742082	Bone
117	VHPC Hands5Phalange right	200	0.048594372	1.065378945	Bone
118	VHPC Heart	1428	0.132789207	1.269775253	Heart Muscle
119	VHPC Hip left	980	0.036646875	2.002544836	Bone
120	VHPC Hip right	988	0.034246882	2.161544262	Bone

Mesh no	Tissue name	Triangle size	Mesh quality	Min. Edge Length	Tissue Type
121	VHPC Humerus left	700	0.090109211	2.071751216	Bone
122	VHPC Humerus right	498	0.034439868	2.581827287	Bone
123	VHPC Intestine	5672	0.036707017	0.447618163	Large Intestine
124	VHPC Jaw	840	0.143250083	1.400989629	Bone
125	VHPC Kidney left	300	0.028643481	2.481834685	Kidney
126	VHPC Kidney right	638	0.041707684	1.216454096	Kidney
127	VHPC L01	674	0.031265386	0.975847616	Bone
128	VHPC L02	586	0.042134673	0.578051374	Bone
129	VHPC L03	578	0.057313192	1.102415462	Bone
130	VHPC L04	766	0.054055214	0.82901676	Bone
131	VHPC L05	942	0.073444425	0.239049863	Bone
132	VHPC L06	632	0.059779006	0.623222465	Bone
133	VHPC LatissimusDorsi left	498	0.040965166	2.743024475	Muscle
134	VHPC LatissimusDorsi right	598	0.078020297	2.610945116	Muscle
135	VHPC Liver	2248	0.034887439	1.660675733	Liver
136	VHPC Lungs	2816	0.007390330	0.741470894	Lungs
137	VHPC Navicular left	100	0.114957833	2.345424348	Bone
138	VHPC Navicular right	150	0.083304334	2.441572668	Bone
139	VHPC Patella left	198	0.089788059	2.201904224	Bone
140	VHPC Patella right	198	0.151620691	2.396437298	Bone
141	VHPC Pectoralis major left	1074	0.030802447	1.358727322	Bone
142	VHPC Pectoralis major right	1394	0.007630889	0.672617027	Bone
143	VHPC Pectoralis minor left	452	0.020491025	1.625624424	Bone
144	VHPC Pectoralis minor right	614	0.082478574	0.958850285	Bone
145	VHPC Peripheral Nerve left	932	0.061059285	2.259336367	Nerves
146	VHPC Peripheral Nerve right	932	0.094532613	1.898872375	Nerves
147	VHPC Pubic Symphysis	250	0.071114943	0.743992045	Bone
148	VHPC Quadriceps left	994	0.032882701	1.931859925	Muscle
149	VHPC Quadriceps right	982	0.031177924	0.67415642	Muscle
150	VHPC Radial Nerve left	444	0.029373803	0.573037251	Nerves
151	VHPC Radial Nerve right	476	0.035138322	0.337814331	Nerves
152	VHPC Ribs Cartilage left1	252	0.032674068	0.10732596	Cartilage
153	VHPC Ribs Cartilage left2	224	0.039296733	0.42635401	Cartilage
154	VHPC Ribs Cartilage left3	240	0.062244747	0.46184925	Cartilage
155	VHPC Ribs Cartilage left4	308	0.050162743	0.302120338	Cartilage
156	VHPC Ribs Cartilage left5	264	0.052634294	0.11539654	Cartilage

Mesh no	Tissue name	Triangle size	Mesh quality	Min. Edge Length	Tissue Type
157	VHPC Ribs Cartilage right left6 9	1886	0.035639113	0.360273388	Cartilage
158	VHPC Ribs Cartilage right1	278	0.031530144	0.088602469	Cartilage
159	VHPC Ribs Cartilage right2	84	0.200369829	1.430276757	Cartilage
160	VHPC Ribs Cartilage right3	192	0.034682883	0.273805472	Cartilage
161	VHPC Ribs Cartilage right4	184	0.096778583	0.95305775	Cartilage
162	VHPC Ribs Cartilage right5	144	0.050570575	0.461775827	Cartilage
163	VHPC Ribs left1	478	0.019485134	0.059519434	Bone
164	VHPC Ribs left2	302	0.036167458	1.169332837	Bone
165	VHPC Ribs left3	424	0.079662765	1.00081454	Bone
166	VHPC Ribs left4	366	0.031003323	1.273279623	Bone
167	VHPC Ribs left5	220	0.033281878	0.64261309	Bone
168	VHPC Ribs left6	404	0.044539529	1.417849603	Bone
169	VHPC Ribs left7	398	0.030545465	0.653095151	Bone
170	VHPC Ribs left8	404	0.035110978	0.47561742	Bone
171	VHPC Ribs left9	464	0.063575806	0.130801175	Bone
172	VHPC Ribs left10	398	0.04119834	1.379307963	Bone
173	VHPC Ribs left11	242	0.067515129	0.731265028	Bone
174	VHPC Ribs left12	154	0.223729357	1.166718734	Bone
175	VHPC Ribs right1	366	0.085075515	0.168269165	Bone
176	VHPC Ribs right2	310	0.058312909	1.220675413	Bone
177	VHPC Ribs right3	512	0.052876232	0.944721096	Bone
178	VHPC Ribs right4	520	0.108244243	0.623120202	Bone
179	VHPC Ribs right5	528	0.141738988	0.93191493	Bone
180	VHPC Ribs right6	512	0.143799299	1.268743582	Bone
181	VHPC Ribs right7	538	0.119547748	0.554086538	Bone
182	VHPC Ribs right8	542	0.037819357	0.530041126	Bone
183	VHPC Ribs right9	590	0.117247699	0.585411056	Bone
184	VHPC Ribs right10	370	0.031070337	1.235435621	Bone
185	VHPC Ribs right11	270	0.073006214	1.17927428	Bone
186	VHPC Ribs right12	188	0.14513063	0.724739586	Bone
187	VHPC Sacrum	3378	0.037207202	1.14952415	Bone
188	VHPC Scapula left	1550	0.032981662	1.222471467	Bone
189	VHPC Scapula right	1430	0.008889689	1.27682971	Bone
190	VHPC Shin left	190	0.040598359	3.141348426	Muscle
191	VHPC Shin right	182	0.032770404	4.385159987	Muscle
192	VHPC Skin Shell	8072	0.024400799	2.002797304	Skin
193	VHPC Skull	3970	0.034021787	1.554063468	Bone

Mesh no	Tissue name	Triangle size	Mesh quality	Min. Edge Length	Tissue Type
194	VHPC Spinal Cord Cauda Equina	2094	0.009146166	0.568865681	Nerves
195	VHPC Spleen	1798	0.059541588	0.57932403	spleen
196	VHPC Sternum	516	0.064846782	1.32325086	Bone
197	VHPC Stomach	1740	0.030579664	1.531579372	Stomach
198	VHPC T01	730	0.049906139	0.478887212	Bone
199	VHPC T02	680	0.03990355	0.298575719	Bone
200	VHPC T03	776	0.03365969	0.199225005	Bone
201	VHPC T04	720	0.037983713	0.151384535	Bone
202	VHPC T05	658	0.031794721	0.194158623	Bone
203	VHPC T06	658	0.051027467	0.302841816	Bone
204	VHPC T07	608	0.127693094	0.547273749	Bone
205	VHPC T08	610	0.040771359	0.517003953	Bone
206	VHPC T09	606	0.069917591	0.499666463	Bone
207	VHPC T10	508	0.120415766	0.778286766	Bone
208	VHPC T11	770	0.083280487	0.69658548	Bone
209	VHPC T12	520	0.135493677	0.598208583	Bone
210	VHPC Talus left	400	0.055791093	1.785631372	Bone
211	VHPC Talus right	398	0.043578315	1.93066917	Bone
212	VHPC Teeth lower17	78	0.039648748	0.838018245	Bone
213	VHPC Teeth lower18	64	0.145539437	1.103929433	Bone
214	VHPC Teeth lower19	54	0.199918551	0.915556673	Bone
215	VHPC Teeth lower28	60	0.294283651	1.034492368	Bone
216	VHPC Teeth lower29	58	0.199512027	0.801353685	Bone
217	VHPC Teeth lower30	64	0.169040286	1.032810707	Bone
218	VHPC Teeth lower31	70	0.034725654	0.629209041	Bone
219	VHPC Teeth upper2	46	0.336087364	1.035037424	Bone
220	VHPC Teeth upper3	44	0.562165632	1.28123595	Bone
221	VHPC Teeth upper4	44	0.555282439	1.174819593	Bone
222	VHPC Teeth upper5 6	26	0.222612812	0.923391582	Bone
223	VHPC Teeth upper7 8	42	0.251937472	1.063572392	Bone
224	VHPC Teeth upper9 10	44	0.316995677	0.674394227	Bone
225	VHPC Teeth upper11	38	0.305477836	0.834837476	Bone
226	VHPC Teeth upper12	36	0.323637235	0.94828928	Bone
227	VHPC Teeth upper13	40	0.396025257	0.952625623	Bone
228	VHPC Teeth upper14	38	0.222425287	1.315784407	Bone
229	VHPC Teeth upper15	46	0.4536344	1.062610605	Bone
230	VHPC Teeth upper16	42	0.518103386	1.365299793	Bone
231	VHPC Tibia left	378	0.032091759	2.359306713	Bone

Mesh no	Tissue name	Triangle size	Mesh quality	Min. Edge Length	Tissue Type
232	VHPC Tibia right	292	0.034509775	4.441764443	Bone
233	VHPC Tongue	188	0.035339146	2.139528992	Tongue
234	VHPC Trabecular lower left	300	0.058536892	1.294933833	Bone
235	VHPC Trabecular lower right	292	0.036315636	2.94324243	Bone
236	VHPC Trabecular upper left	248	0.05526317	2.531759578	Bone
237	VHPC Trabecular upper right	296	0.074769073	2.503679206	Bone
238	VHPC Trachea Sinus	1150	0.031995125	0.167170914	Air
239	VHPC Trapezious left	208	0.063185887	3.199869554	Muscle
240	VHPC Trapezious right	216	0.041968499	2.524350576	Muscle
241	VHPC Ulna Radius left	684	0.032459185	1.73710088	Bone
242	VHPC Ulna Radius right	682	0.032006196	1.559339319	Bone
243	VHPC Ulnar Nerve left	476	0.020694248	0.571556062	Nerves
244	VHPC Ulnar Nerve right	476	0.032384549	0.517344222	Nerves
245	VHPC Uterus	494	0.035017825	1.498865329	Uterus
246	VHPC Veins lower	5464	0.003923694	0.20214316	Blood
247	VHPC Veins upper	6422	0.013610025	0.419059576	Blood
248	VHPC WhiteMatter	1946	0.031200425	0.971308067	Brain (White Matter)

2.4.2 Peripheral Nervous System and Cardiovascular System

The new version VHP-Female v.3.1, as shown in figure 2.4 includes a state of the art peripheral nervous system which currently comprises of the radial, median, ulnar (brachial plexus), and sciatic nerves (sacral plexus) segmented over large lengths. The inclusion of cauda equina along with the brachial plexus and sacral plexus is the first of its kind, a unique feature of the VHP-Female v3.1 model. This peripheral nervous system can be used to study and model various electrical stimulation systems operating on peripheral nerves. Note that a high-resolution human-head model developed in [7] has the detailed representation of twelve cranial nerves.

Figure 2.5 shows the graphical cartoon representations of the sciatic nerve, as well as radial, median, and ulnar nerves along with the corresponding anatomical counterparts identified in the cryosection images from the VHP-Female image dataset. The nerve tissues were registered and segmented via segmentation algorithms developed in MATLAB. The final triangular tissue mesh structure was built upon the existing point cloud, in the form of connective cylindrical elements with varying radii and lengths. The traditional ball-pivoting algorithm is not effective; it generated results with a low mesh quality since the nerves are extremely thin as compared to other tissues.

Table 2.2 Existing nervous tissues and other nervous tissues considered for future development

Tissue Name	**Triangle Size**	**Mesh Quality**	**Minimum Edge Length**
Median Nerve left	520	7.14E-7	0.39E-3
Median Nerve Right	492	5.24E-4	0.64
Sciatic Nerve left	946	9.63E-4	0.60
Sciatic Nerve right	932	7.23E-2	0.59
Radial Nerve left	762	8.24E-6	0.03
Radial Nerve right	476	2.66E-3	0.34
Ulnar Nerve left	476	1.90E-2	0.57
Ulnar Nerve right	540	4.51E-	0.02
Peroneal Nerve left Peroneal Nerve right Femoral Nerve left Femoral Nerve left Saphenous Nerve left Saphenous Nerve right	Under development		

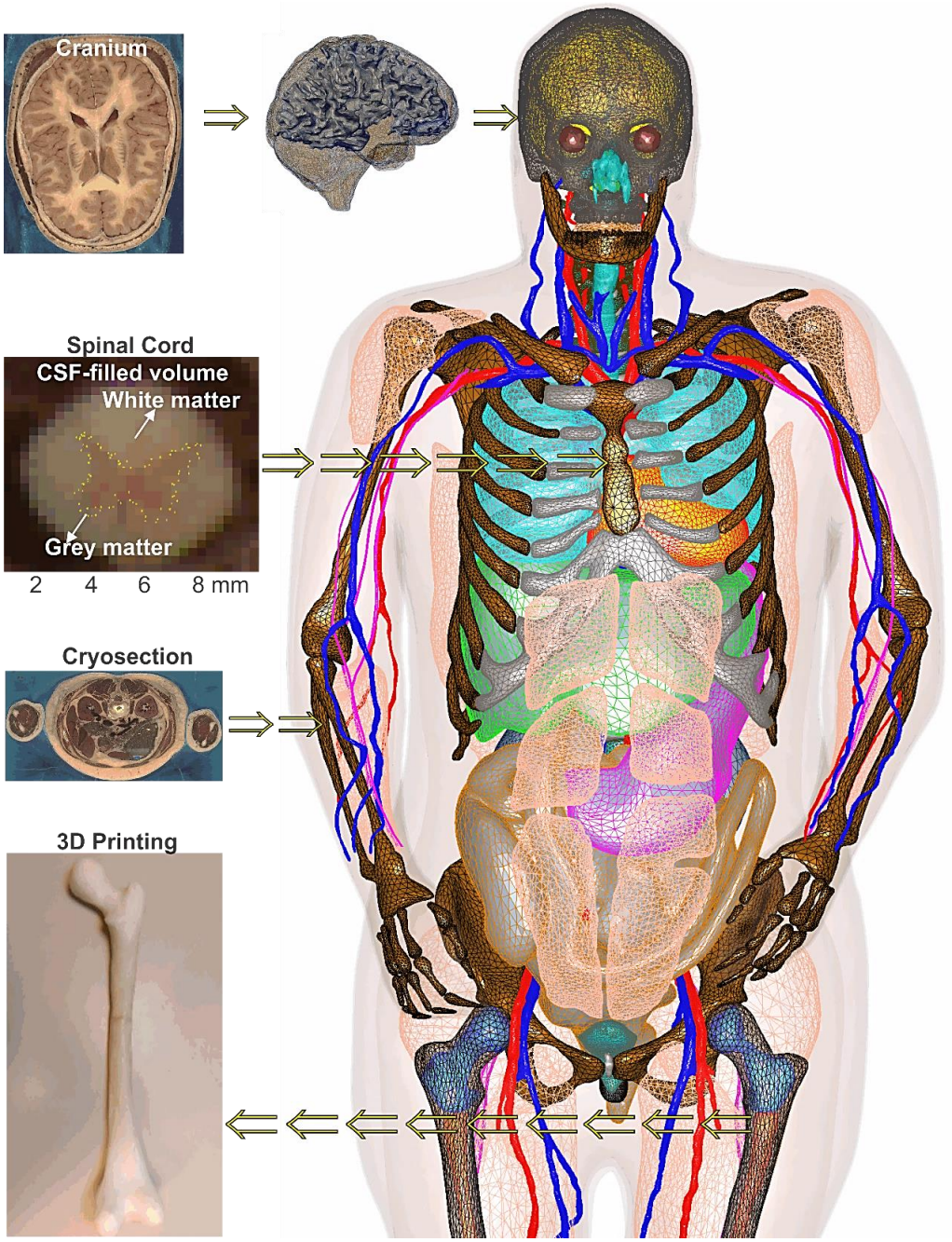

Figure 2.4 Anterior view of the VHP-Female computational smooth model v. 3.1 within MATLAB. Illustration of tissue object development from cryosection images and 3D printed femur model is shown. Fat and some muscles are not shown in VHP-Female v. 3.1.

2.4.3 Muscular System

Along with the heart muscle, the muscular system includes major skeletal muscles (33 in total) in the form of separate objects. All muscle objects are contained within the average body object depicted in Figure.2.6. Table 2.3 summarizes the muscle and other enhancements in VHP-Female v.3.1 as compared to VHP-Female v.2.0.

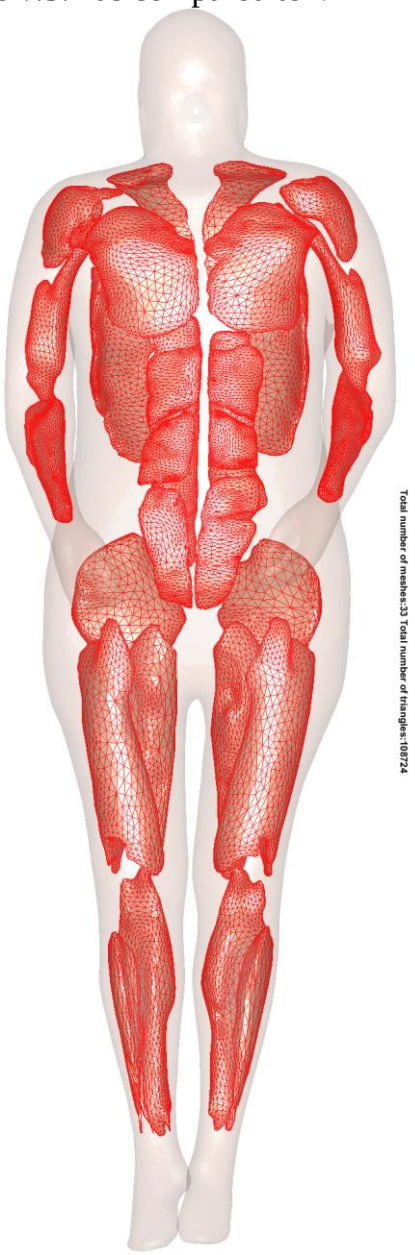

Figure 2.6 Muscular system with total number of meshes: 33 , Total number of triangles: 108724

TABLE 2.3. MAJOR IMPROVEMENTS IN VHP-FEMALE V. 3.1

List of improvements	
1	Development of sciatic nerve, ulnar nerve, radial nerve, and median nerve for the right and left sides, respectively (state-of-the-art). Addition of spinal cord cauda equina.
2	Expansion of systemic venous system.
3	Addition of erector spinae left and erector spinae right.
4	Addition of pectoralis major left, pectoralis major right, pectoralis minor left, and pectoralis minor right.
5	Addition of abdominals left bottom, abdominals left middle, abdominals left top, abdominals right bottom, abdominals right middle, and abdominals right top.
6	Improvement of ribs left2, ribs left7, ribs left8, ribs left9, ribs right2, ribs right7, ribs right8, and ribs right9 along with respective cartilages. Separation of clavicle left, clavicle right from the rib cage.
7	Development of forearm flexors left and right, respectively.
8	Anatomical accuracy of Gray matter/White Matter /intestine/bladder improved.
9	Development of spleen.
10	Sharp corners have been smoothed, which improves the numerical accuracy.

2.4.4 Smoothed Model and Base Model

The VHP-Female v.3.1 model includes two versions: BASE (~160,000 facets) and SMOOTH (a smoothed version for more accurate SAR calculation with ~640,000 facets). The corresponding doi numbers (related to version 3.0) are as follows:
DOI:10.20298/VHP-Female-V.3.0-BASE
DOI:10.20298/VHP-Female-V.3.0-SMOOTH

The BASE and SMOOTH versions of the model have the same number of tissues and identical topology. The corresponding surface deviation between the two models does not exceed 0.2-1 mm on flat surfaces, but may be as high as 2-7 mm for sharp edges and corners.

During electromagnetic simulations the surface charge density formally becomes singular at any edge (not necessarily sharp) of a triangular mesh with non-planar triangles. For sharper edges and large adjacent triangles, this local (electrostatic) effect becomes quite significant and may lead to non-physical field/current peaks [8]. This deficiency has been addressed in the smooth version.

2.4.5 Other Improvements

The latest unique features of the VHP-Female v.3.1 include 1 mm resolution in the cranium and a continuous cerebrospinal fluid (CSF) shell, 0.5 mm state-of-the-art resolution in the spinal cord, segmentation of long peripheral nerves visible in cryosection images, segmentation of individual muscles, and three full-body shells: skin, fat, and average body .The VHP-Female v.3.1 features and the 3D tissue objects have been evaluated by a number of medical doctors from Beth Israel Deaconess Med. Center, Harvard Med. School, Boston, MA. Anatomical and numerical improvements including but not limited to rib cage, venous system, intestine, and bladder have been done.

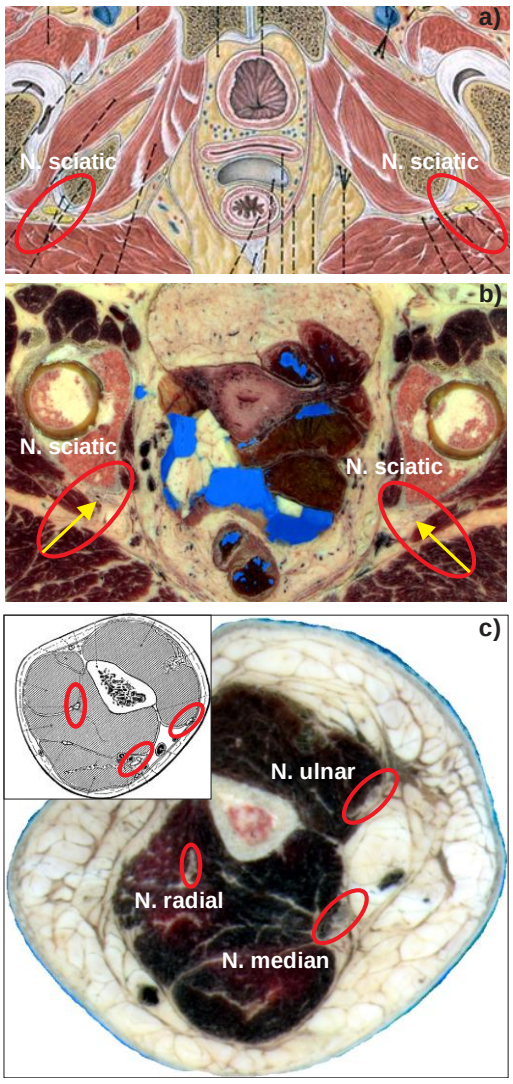

Figure 2.5 a) Graphical representation of sciatic nerves in the lower pelvic region; b) Illustration of sciatic nerves in the cryosection image from the original dataset; c) Graphical and realistic illustration of radial, median, and ulnar nerves in the forearm region

2.5 General Application of the human phantom.

2.5.1 Respiratory Motion

An approximate method to conveniently model respiratory motion for VHP-Female v. 3.1 human model in a commercial FEM solver has been suggested and realized. Its idea is in using only native embedded affine transformations and an elaborate parametric sweep for all involved objects simultaneously, as a function of one single variable – time. The sweep sequence is constructed and optimized separately. The optimization goal is to follow anatomical respiration as close as possible while avoiding intersections between nearby objects at every time step. This method does not require using multiple model copies.

This application has been developed by Mr. Tran in his thesis [16]

References

[1]. IEEE International Committee on Electromagnetic Safety: Technical Committee 34: List of available human phantoms: http://grouper.ieee.org/groups/scc34/sc2/wg2/available%20human%20models.doc

[2]. K. Genc, P. Segars, S. Cockram, D. Thompson, M. Horner, R. Cotton, and P. Young, "Workflow for creating a simulation ready virtual population for finite element modeling," in 2013 Proc. ASME/FDA 1st Annual Frontiers in Medical Devices: Applications of Computer Modeling and Simulation, FMD2013, Sep. 11-13, 2013, Washington, DC.

[3]. A. Christ, W. Kainz, E. G. Hahn, K. Honegger, M. Zefferer, E. Neufeld, W. Rascher, R. Janka, W. Bautz, J. Chen, B. Kiefer, P. Schmitt, H.-P. Hollenbach, J. Shen, M. Oberle, D. Szczerba, A. Kam, J. W. Guag, and N. Kuster, "The Virtual Family - development of surface-based anatomical models of two adults and two children for dosimetric simulations," Phys. Med. Biol., vol. 55, pp. N23-N38, Jan. 2010.

[4]. M. C. Gosselin, E. Neufeld, H. Moser, E. Huber, S. Farcito, L. Gerber, M. Jedensjö, I. Hilber, F. Di Gennaro, B. Lloyd, E. Cherubini, D. Szczerba, W. Kainz, and N. Kuster, "Development of a New Generation of High-Resolution Anatomical Models for Medical Device Evaluation: The Virtual Population 3.0," Phys. Med. Biol., vol. 59, no. 18, pp. 5287-5303, online August 21, 2014.

[5]. X. G. Xu and K. F. Eckerman, Handbook of Anatomical Models for Radiation Dosimetry. Boca Raton: Taylor & Francis, 2010.

[6]. U.S. National Library of Medicine. The Visible Human Project® Online: http://www.nlm.nih.gov/research/visible/visible_human.html

[7]. M. Iacono et al., "MIDA: A Multimodal Imaging-Based Detailed Anatomical Model of the Human Head and Neck," PLoS ONE, vol. 10, no 4, online April 22, 2015.

[8]. S. N. Makarov et al., "Preliminary Upper Estimate of Peak Currents in Transcranial Magnetic Stimulation at Distant Locations from a TMS Coil," IEEE Trans. Biomedical Engineering, vol. 64, accepted. Early access: http://ieeexplore.ieee.org/xpl/articleDetails.jsp?arnumber=7352318&filter%3DAND%28p_IS_Number%3A4359967%29

[9]. N. Han et al., "Electrical stimulation does not enhance nerve regeneration if delayed after sciatic nerve injury: the role of fibrosis," Neural Regeneration Research, vol. 10, no. 1, pp. 90–94, Jan. 2015.

[10]. N. Berardoni et al., Sciatica Treatment and Therapy [Online], Available FTP: http://arizonapain.com/pain-center/pain-treatments/sciatica/

[11]. A. S. L. Leoni et al., "High voltage pulsed current stimulation of the sciatic nerve in rats: analysis by the SFI," Acta Ortopedica Brasileira, vol. 20, no. 2, pp. 93–97, Mar. 2012.

[12]. J. Yanamadala et al, “Multi-Purpose VHP-Female Version 3.0 Cross-Platform Computational Human Model,”10th European Conference on Antennas and Propagation 2016 (EuCAP16), Davos, Switzerland, April 2016.
[13]. IT IS database: http://www.itis.ethz.ch/virtual-population/
[14]. J. Yanamadala, “Development of Human CAD Models and Related Mesh Processing Algorithms with Application in Bio electromagnetic” Dissertation, April 2016.
[15]. Giaccari Luigi, “http://giaccariluigi.altervista.org/blog/”
[16]. Anh Le Tran, “Development of the VHP Female CAD model including Dynamic Breathing Sequence”, Thesis, Dept. Elect. and Computer Eng., Worcester Poly. Inst., April 2017.

Chapter 3

Validation of CAD Human Phantoms

3.1 Introduction

It is extremely important that during the process of creating numerically efficient meshes, the anatomical accuracy is not significantly compromised. This calls for rigorous testing of the CAD human model. Since the VHP-Female dull body model is subject to Food and Drug Administration (FDA) Medical Devices Development Tool (MDDT) Qualification as a non-clinical assessment model, it needs to be validated thoroughly.

The VHP-Female v. 3.1 model is validated under the categories as listed below. Anatomical accuracy and realistic simulation results would validate this model to be used for establishing safety standards. The human anatomy of the phantom relates to the age group of 50 to 65-year-old female patients. The BMI range is from 30-35 which signifies over-weight to obese group.

The categories of validation are as follows:

1. Anatomical Segmentation Validation by Medical Professionals
2. Segmentation Validation by image Co-Registration
3. Computer Aided (CAD Validation)
4. Electromagnetic Validations (MRI)

This Chapter gives an insight towards the validation of CAD human phantoms which sets a benchmark for validation of such models.

3.2 Visual Inspection by Medical Professionals

The general anatomical accuracy of the model has been inspected and corrected by a committee of medical experts including Dr. A. Nazarian, Dr. F. Fregni, Dr. A. R. Opotowsky, Dr. G. Haleblian, Dr. V. Poylin, Dr. J. Wilson, Dr. E. K. Rodriguez, Dr. A. Pascual-Leone, Dr. A. Nummenmaa (all from Harvard Med. School, Boston, MA), Dr. M. Kozlov, Dr. N. Weiskopf, PD Dr. S. Geyer (all from Max Planck Inst. for Human Cognitive and Brain Sciences, Germany), and Dr. P. Riahi (Biotronik & Micro Sys. Eng., Inc.).

This visual inspection has greatly driven the progress of the CAD phantom. In summary, corrections have been made to about 40 anatomical and numerical flaws including anomalies in the original image dataset. An example of this is given by a dark-colored volume that exists between the cranium and the scalp, which has been classified as an artifact. Such a volume likely appeared as a result of the freezing procedure.

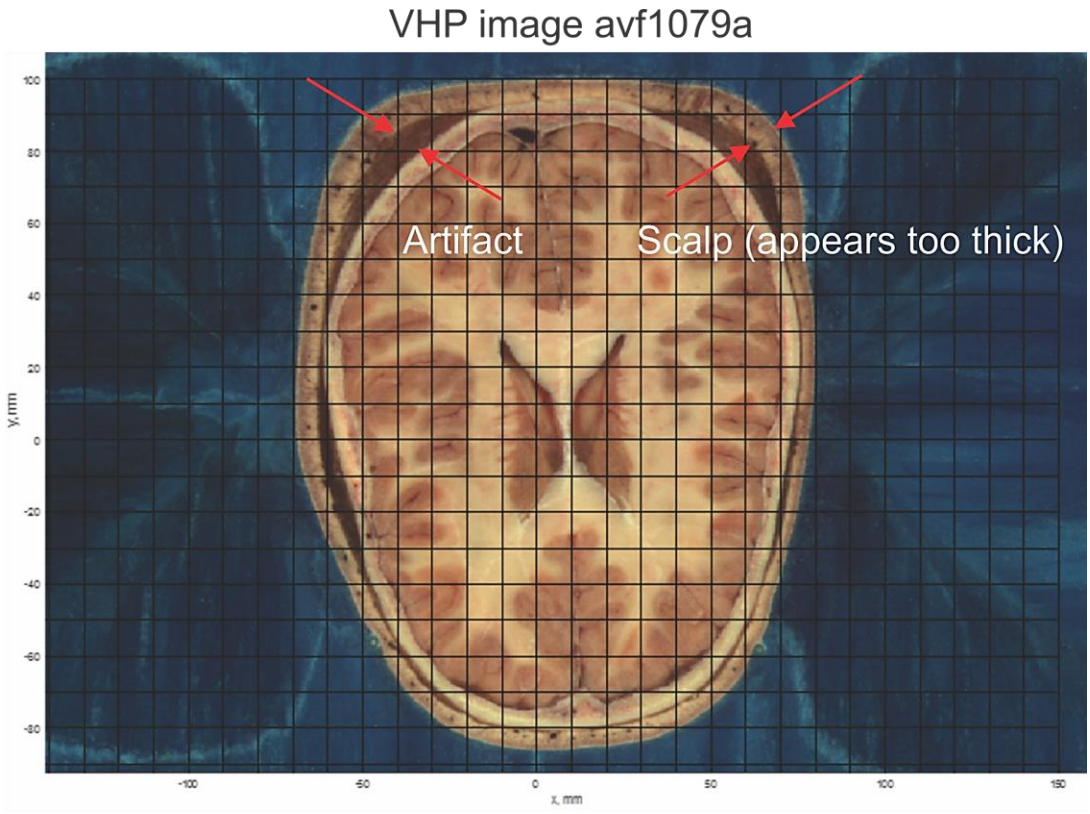

Figure 3.1 Artifact in the VHP-Female dataset

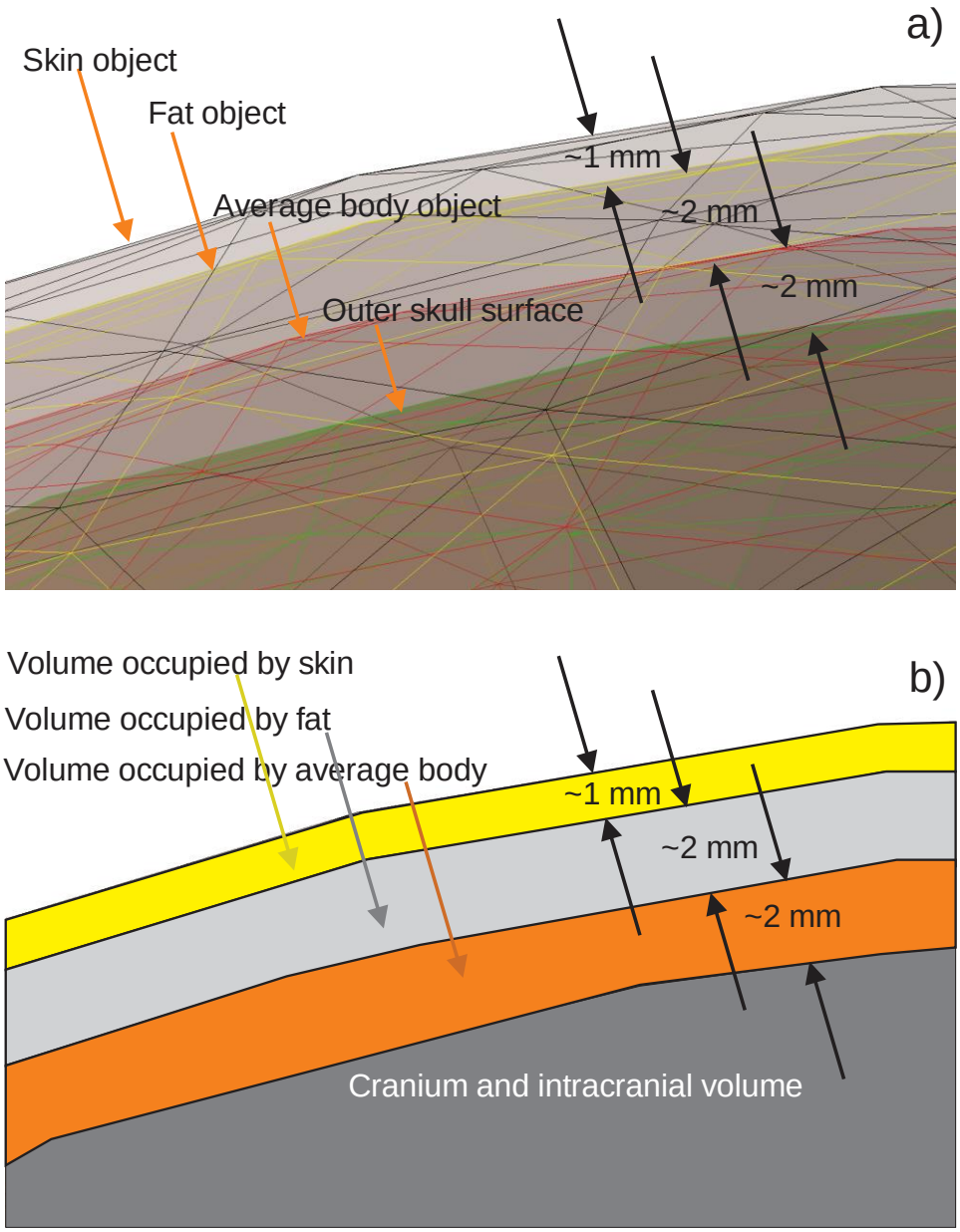

Figure 3.2 Justification of the artifact in the image

3.3 Segmentation Validation by co-registration

Now, with custom MATLAB tools, the cryosection images that were segmented to create triangular meshes can be examined. These meshes were processed in various mesh processing packages such as ANSYS SpaceClaim, meshmixer and MeshLab. In the process of healing the meshes and making them geometrically robust, the anatomical accuracy should not be compromised. To check this fact, we superimpose the tissue onto the respective cross sectional image.

Within 1mm accuracy, through visual inspection, can establish a strong correlation between the anatomical accuracy of the segmented tissue with respect to the cross sectional image. The figure below shows this overlay of the tissue on the image. This process involves the extraction of the *x, y* coordinates for a particular slice in the *z* direction followed by overlaying them onto the image corresponding to that particular *z* location.

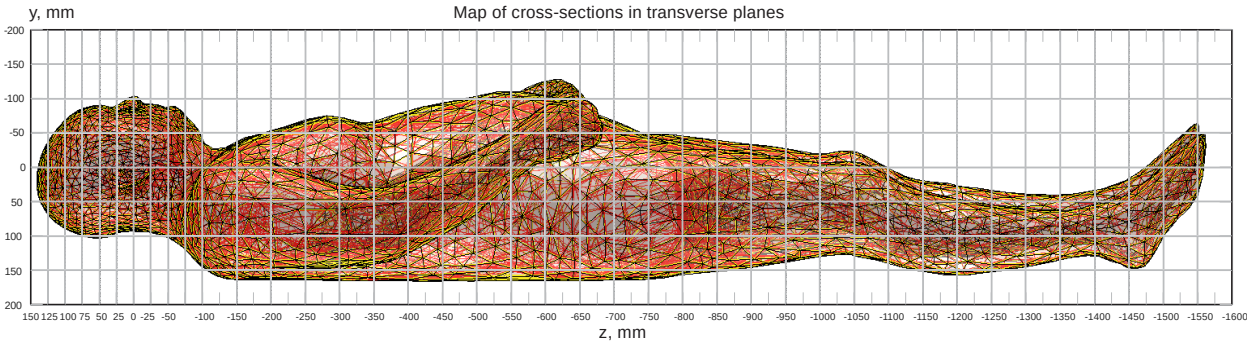

Figure 3.3 Map of cross-section in transverse planes.

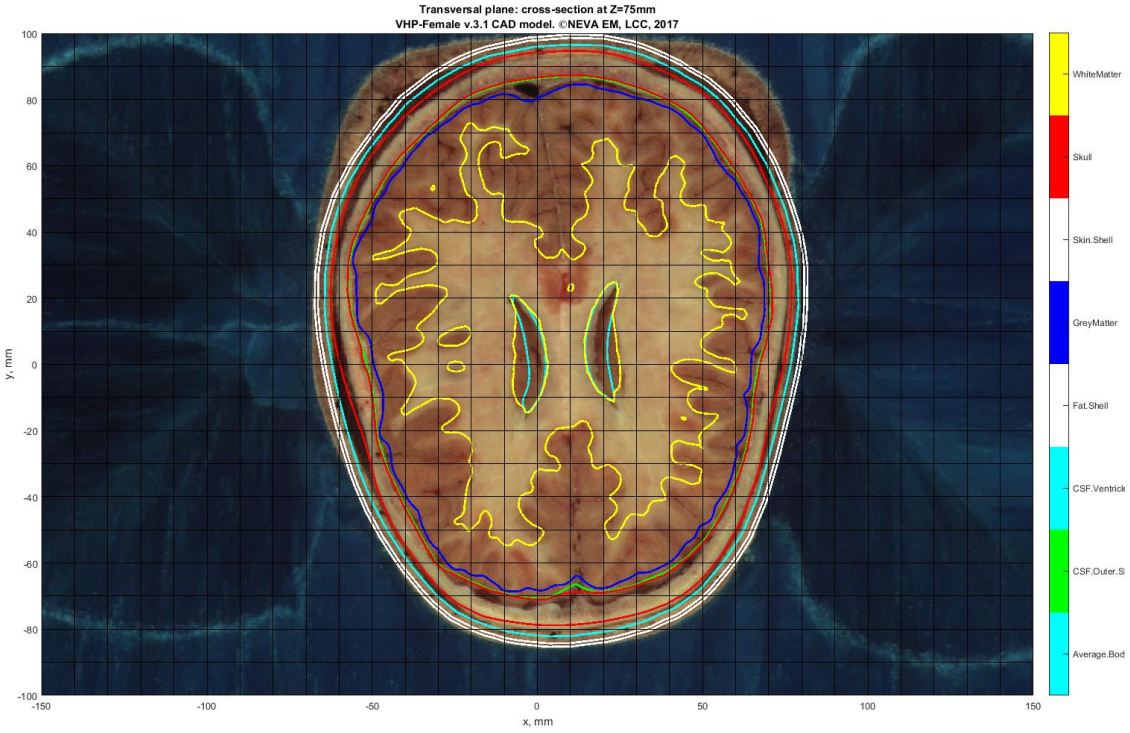

Figure 3.4 Example#1 Head, Z= +75 mm

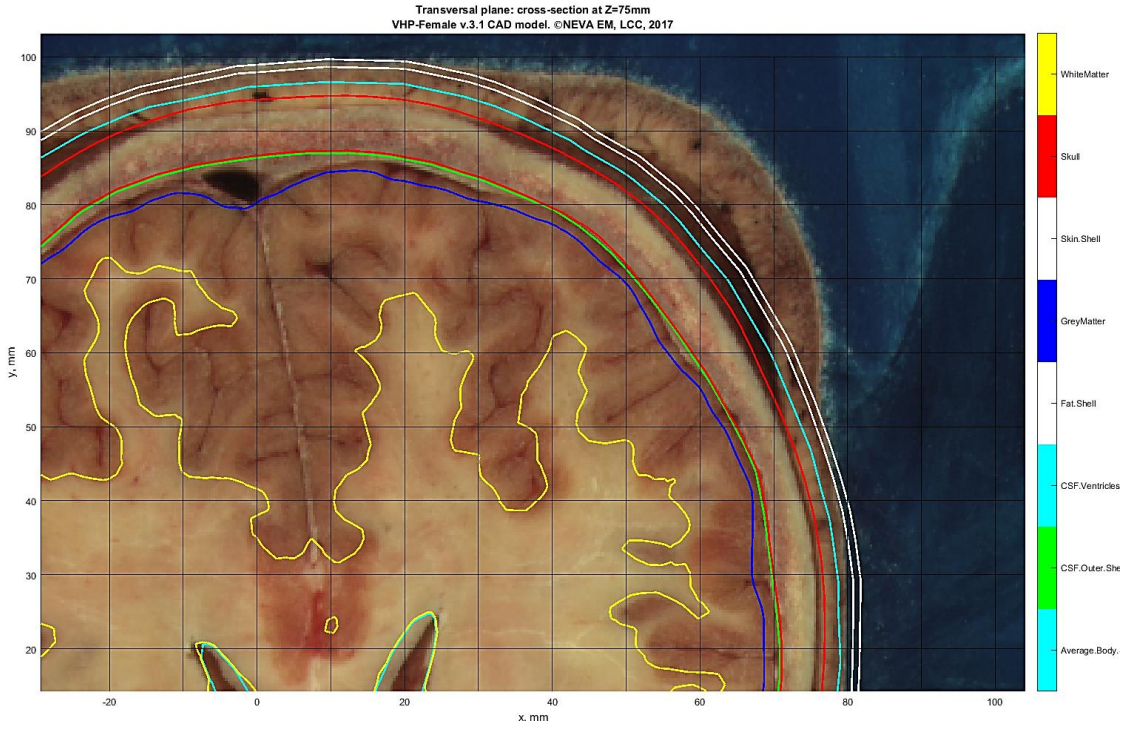

Figure 3.5 Example#2 Head, Z= +75 mm, magnified to show interior detail

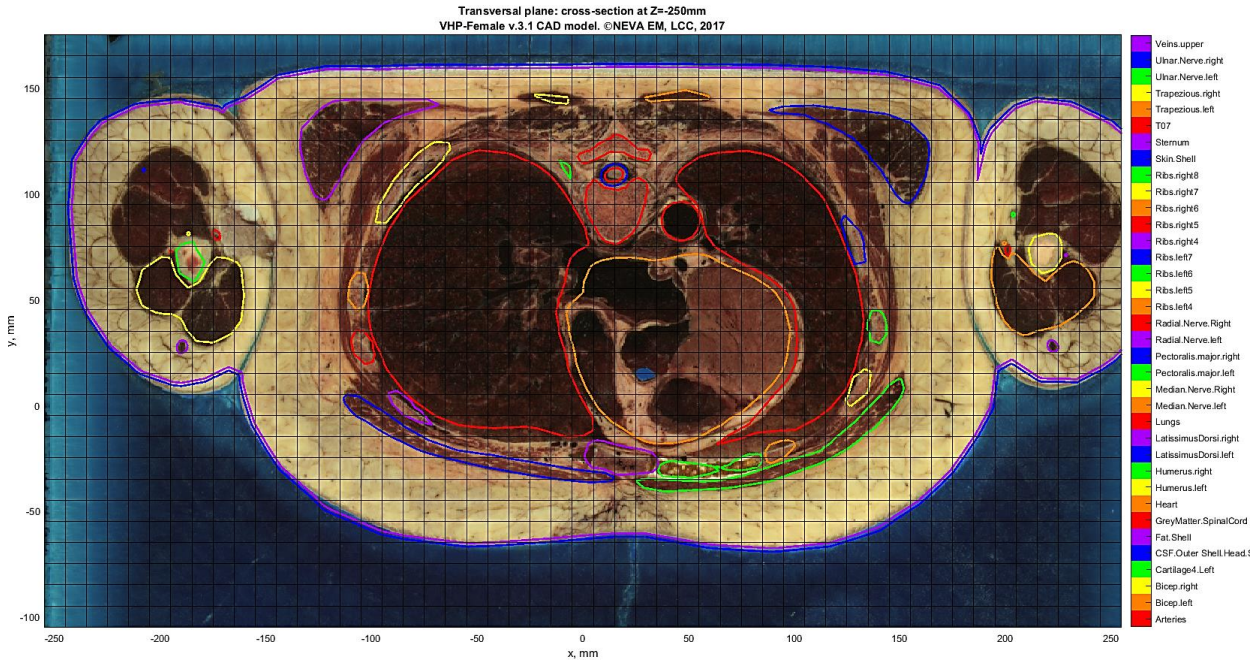

Figure 3.6 Example#3 Body, Z= -250 mm

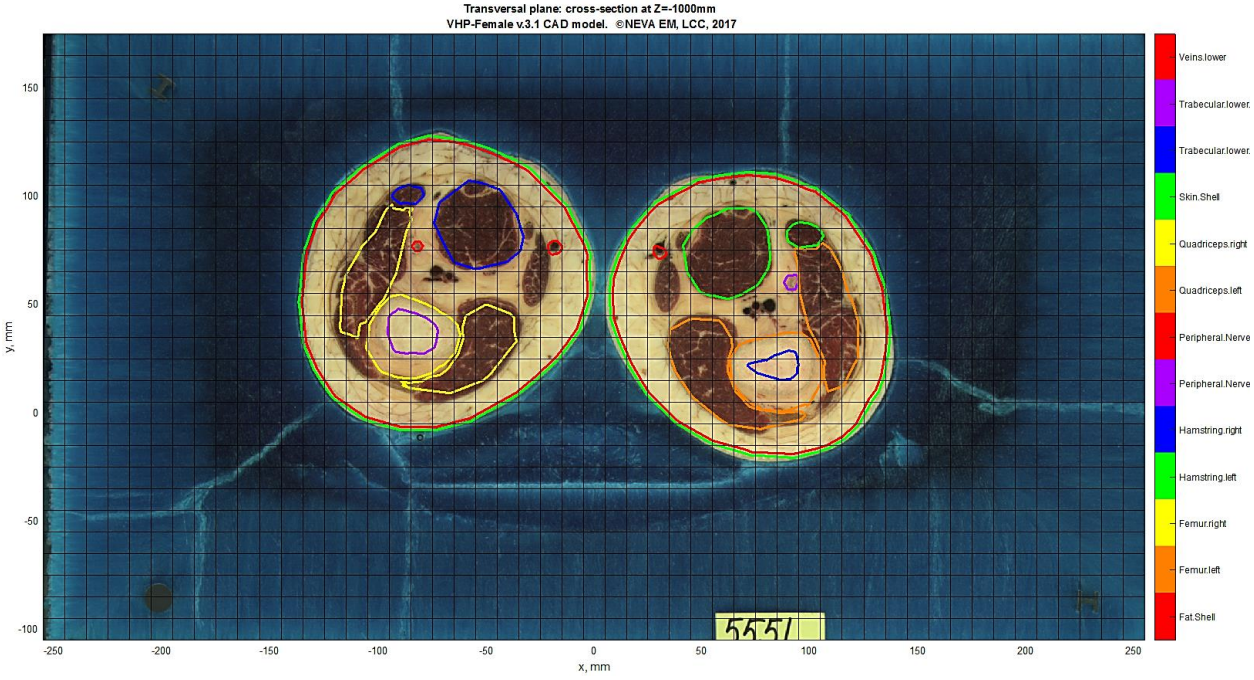

Figure 3.7 Example# 4 Legs, Z= -1000 mm

3.4 Computer Aided Design (CAD) validation

The test to determine the geometrical accuracy of the CAD phantom tissues is performed here. The tissue objects must be 2-manifold, without self-intersections or intersections with nearly objects.

The meshes can be tested in MATLAB®, using custom scripts, optical tools such as MeshLab, ANSYS SpaceClaim or commercial CEM packages. All commercial CEM packages have boolean operation tools available.

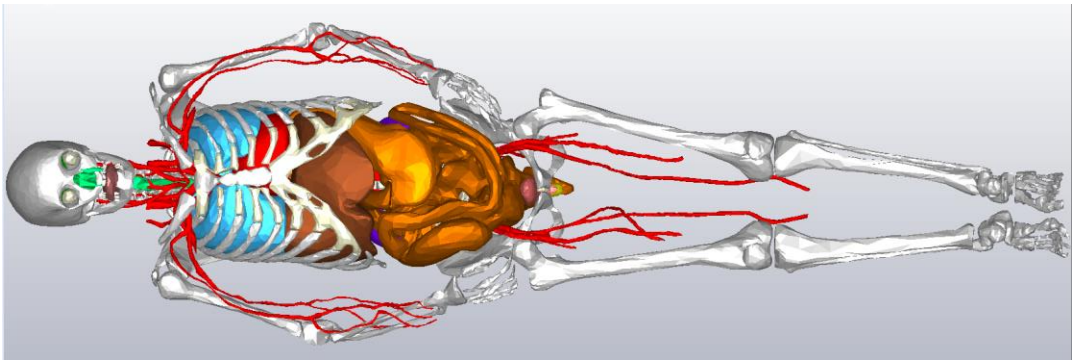

Figure 3.8 The VHP-Female model in Computer Simulation Technology (CST) package

3.5 Electromagnetic Validation

Virtually every modern commercial biomedical electromagnetic device must receive an FDA approval prior to going to market. This approval requires rigorous testing to ensure the safety of the patient as well as the operator. Such devices include magnetic resonance (MR) imaging coils, Electroencephalography (EEG), Electrocardiography (ECG), and Magnetoencephalography (MEG) devices, brain-computer interfaces, MR conditional passive or active implanted devices, neuro-stimulators and electrical stimulators, devices for radio frequency ablation and radio-frequency cancer treatment, cellphone antennas, on-body and implanted antennas for body-area sensor networks, and endoscopic video capsules communicating via radio frequency (RF) signals.

Current regulatory procedures require determination of the Specific Absorption Rate or SAR. However, SAR measurements are not easily performed for human subjects *in-vivo and* are typically derived from simulations performed with *virtual humans*. The concept and theory behind SAR calculations is discussed in section 3.5.3.1

This section is organized into two major topics. First, the development of a *complete generic computational workflow* for testing virtual humans in an RF transmit coil is presented. Second, application of *this workflow to* the *VHP-Female model* and established a *good agreement* with the known literature data with regard to SAR evaluations.

The workflow outputs a volumetric distribution of the right-handed circularly-polarized RF magnetic field $\boldsymbol{B}_1^+$. This field is responsible for exciting proton spins. The workflow also outputs a volumetric distribution of Specific Absorption Rate including

a. Whole-body SAR
b. Non-averaged local SAR with the voxel size of 1 mm^3 or 2 mm^3
c. Maximum 1g SAR (SAR_{1g}) averaged over the volume contained in 1 g
d. Maximum 10g SAR (SAR_{10g}) averaged over the volume contained in 10 g

Once the computed data is within certain standard margins, the human model may be considered an acceptable tool for regulatory radio frequency simulations and safety evaluations.

The key point of the approach is a novel concept of an ideal (perfectly matched and tuned) RF transmit coil, which essentially bypasses the coil matching procedure and does not require the circuit co-simulator. This concept has been thoroughly validated in the study.

3.5.1 New "Universal" (Perfectly Tuned & Matched) RF Transmit Coil Model

As a base RF transmit test coil, we will consider the *simple generic high-pass birdcage coil* shown in Figure 3.1. The coil has 16 rungs and 32 matching capacitors; it is fully parameterized. Every matching capacitor may also represent *a port* as described below. The coil can be easily scaled to be used either for the head or as a full-body coil of a varying size. Other topologies may be handled similarly.

The entire problem is very complex since RF coil designs vary widely. Furthermore, RF coils need to be *tuned* and their ports need to be *matched*. The foundations of RF coil tuning and matching are given in Refs.[1]-.[15] An accurate tuning and matching procedure requires two distinct software packages: a *full-wave CEM simulator* coupled with a *circuit co-simulator* for multiport circuit modeling (with up to 64 ports for modern RF coils. A ***novel generic approach*** is presented, which essentially bypasses the matching procedure and *does not* require the circuit co-simulator. The idea consists of the design and usage of an "ideal" coil model, which is already "perfectly" tuned and matched at all ports. Such a concept will be disclosed below.

The birdcage coil used here is a high pass birdcage coil. We are using a 1.5T coil. The resonant frequency here is 63.87 MHz. Further discussion about Larmor Frequency is conducted in the following subsection.

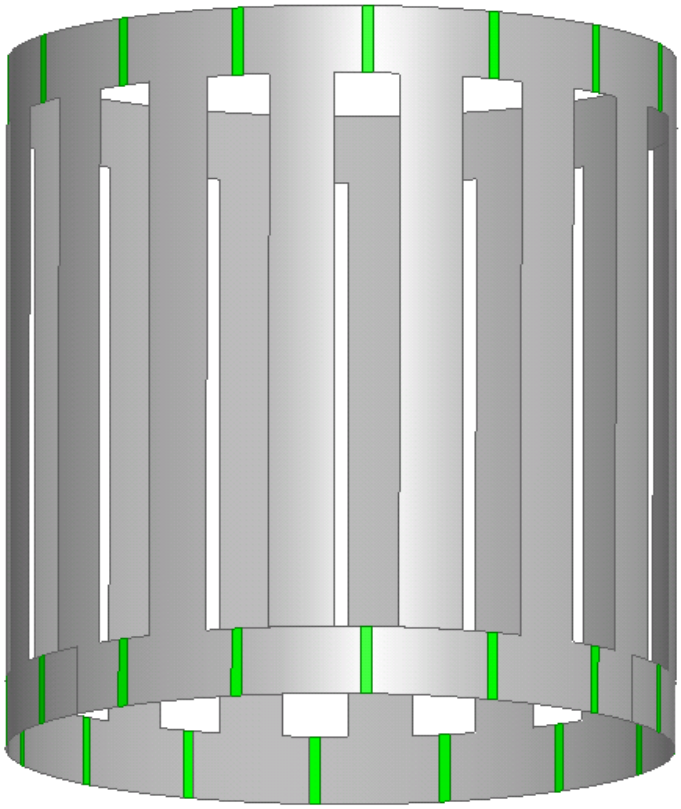

Figure 3.9 A generic high-pass birdcage MRI RF coil used in simulations. Tuning capacitors and/or driving ports are marked green.

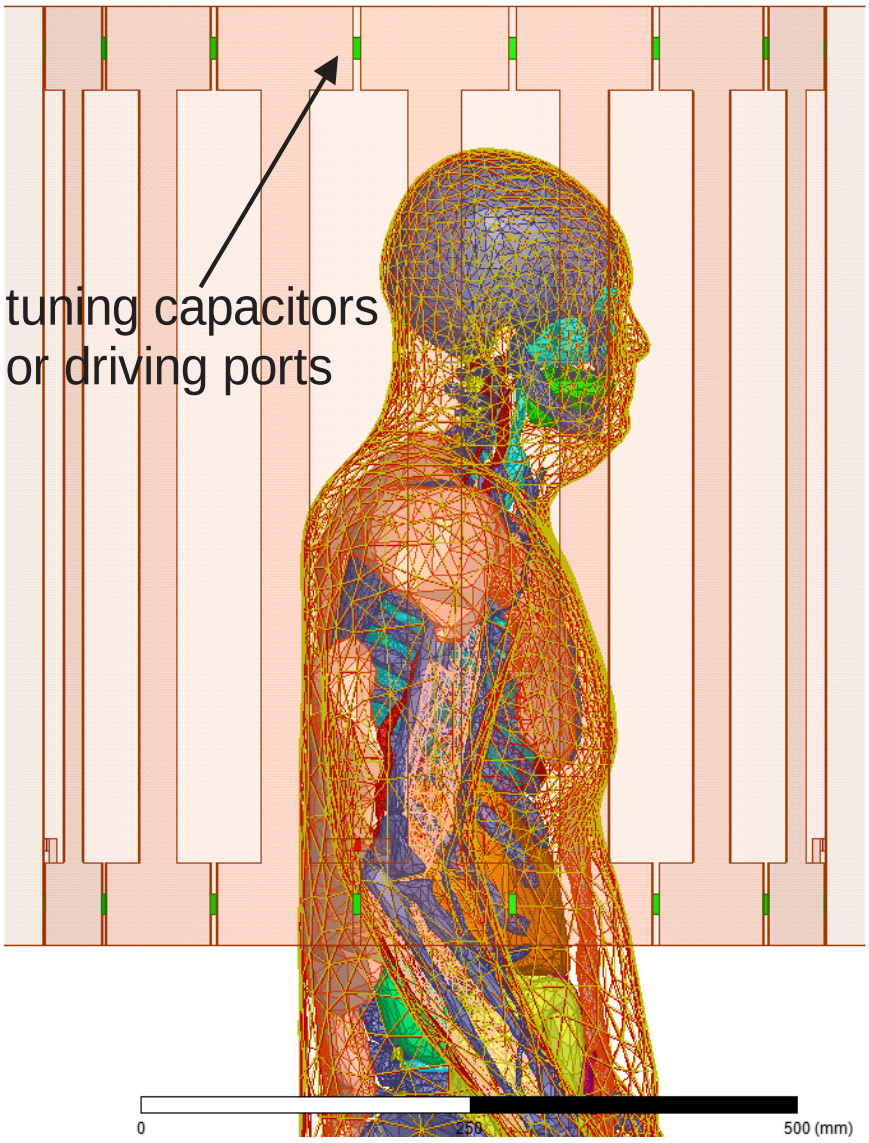

Figure 3.10 VHP-Female model v.3.0 BASE in another full-body high-pass birdcage MRI RF coil.

Step 1. *RF coil as a resonator.* Any RF MRI coil such as the most common high-pass birdcage coil shown in **Figure 3.9** above and in **Figure 3.10** is a familiar *LC resonator*. The inductance L ("mass") is due to vertical coil conductors (rungs) seen in **Figures 3.9** and **3.10,** while the capacitance C (inverse "stiffness") is due to the lumped tuning capacitors marked green in **Figures 3.9** and **3.10**. The number of distinct coil resonances is *equal* to the number of the tuning capacitors ("springs") in **Figures 3.9** and **3.10**. The resonances appear *in pairs* exactly corresponding to the pairs of upper and lower capacitors in **Figures 3.9** and **3.10**. Magnetic fields of each pair of resonant models are *perpendicular* to each other. When combined, these two perpendicular fields make it possible to create *a circular polarization.*

Step 2. *Finding all coil resonances.* In order to find all resonances of the coil and then select *the main resonant mode pair*, we will consider the coil in **Figures 3.9** and **3.10** as a generic *N*-port linear network shown in **Figure 3.11**. *Every* tuning capacitance C_0 (with an impedance of Z_0 at *the a priori known* resonant frequency) is now becoming an *independent port* driven by an RF generator. The *N*-port network is routinely modeled in any commercial CEM software at the known resonant frequency. As a result, an *impedance matrix* $\hat{\boldsymbol{Z}}$ is obtained, which relates the port voltages $\vec{\boldsymbol{V}}$ and currents $\vec{\boldsymbol{I}}$ by:

$$\begin{bmatrix} V_1 \\ V_2 \\ \dots \\ V_N \end{bmatrix} = \begin{bmatrix} Z_{11} & Z_{12} & \dots & Z_{1N} \\ Z_{21} & Z_{22} & \dots & Z_{2N} \\ \dots & \dots & \dots & \dots \\ Z_{N1} & Z_{N2} & \dots & Z_{NN} \end{bmatrix} \times \begin{bmatrix} I_1 \\ I_2 \\ \dots \\ I_N \end{bmatrix} \qquad (1)$$

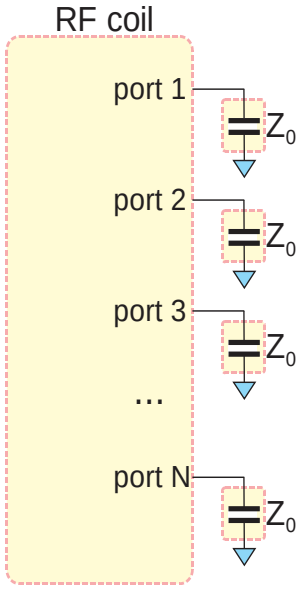

Figure 3.11. RF MRI coil terminated into N ports (with impedances Z_0).

Eq. (1) is nothing more than the expansion of Ohm's law, $V = RI$, to a multiport system. Mathematically, the N distinct coil resonances correspond to N *eigenvalues* and N *eigenvectors* of the impedance matrix $\widehat{\boldsymbol{Z}}$, very similar to the eigenvalues of the stiffness matrix in mechanical engineering of lumped resonant systems. Any eigenvalue is equal to Z_0, i.e., to the port impedance which is the same for all ports, i.e., $\vec{\boldsymbol{V}} = Z_0\vec{\boldsymbol{I}}$. From Eq. (1), the corresponding eigenvalue problem is obtained in the form:

$$\begin{bmatrix} Z_{11} & Z_{12} & \dots & Z_{1N} \\ Z_{21} & Z_{22} & \dots & Z_{2N} \\ \dots & \dots & \dots & \dots \\ Z_{N1} & Z_{N2} & \dots & Z_{NN} \end{bmatrix} \times \begin{bmatrix} I_1 \\ I_2 \\ \dots \\ I_N \end{bmatrix} = Z_0 \begin{bmatrix} I_1 \\ I_2 \\ \dots \\ I_N \end{bmatrix} \qquad (2)$$

We will solve Eq. (2) using MATLAB or another general engineering software package. As a result, we will obtain N resonances: N distinct values of port impedance Z_0 and N distinct values of vector $\vec{\boldsymbol{I}}$ (electric currents at the ports).

Step 3. *Finding two main coil resonances.* The pair of desired resonant modes must generate a magnetic field that is *as homogeneous as* possible within the coil, which is directed along one of the horizontal axes in **Figures 3.9** and **3. 10** (either along the *x*-axis or along the *y*-axis). In this case, the current distribution $\vec{\boldsymbol{I}}$ for every mode in the pair must be a *sinusoidal function of the polar angle φ around the coil with exactly one period*. The corresponding *mode strength*, m, is therefore given by a Fourier coefficient,

$$m = abs\left(\sum_{n=1}^{N/2} \exp(4\pi jn/N)\, I_n\right) \qquad (3)$$

The analysis of mode strength from Eq. (3) will show two nearly equal clear peaks (10-50 times higher than the rest of the values) corresponding to the two desired modes. Yet another approach is to realize that the main resonance is *exactly* at the upper end of the group of coil resonances that lead to positive values of C_0 (with the two largest values of C_0).

Step 4. *Constructing a perfectly matched coil with 1 W total input power.* In practice, only a limited number of ports are driven (typically two or four). In order to obtain a solution *exactly* corresponding to the two resonant modes, we drive *all* ports and assume *ideal matching* to the characteristic impedance Z_c (typically $Z_c = 50\ \Omega$). Given the incident normalized power wave at the ports as $\vec{\boldsymbol{A}} = \vec{\boldsymbol{V}} + Z_c\vec{\boldsymbol{I}}$ and the reflected power wave as $\vec{\boldsymbol{B}} = \hat{\boldsymbol{S}}\vec{\boldsymbol{A}}$, where $\hat{\boldsymbol{S}}$ is the known scattering matrix (expressed through the impedance matrix and vice versa), we find the total input power per mode $i = 1,2$ as

$$P_i = 1/2\left(\left|\vec{\boldsymbol{A}}\right| \cdot \left|\vec{\boldsymbol{A}}\right| - \left|\vec{\boldsymbol{B}}\right| \cdot \left|\vec{\boldsymbol{B}}\right|\right) \qquad (4)$$

The normalized main mode is $\vec{\boldsymbol{A}} = \vec{\boldsymbol{A}}/\sqrt{2P_i}$. Finally, a right-handed circularly-polarized magnetic field $\boldsymbol{B}_1^+$ with 1 W total input power will be generated by the port sources $\vec{\boldsymbol{S}} = \vec{\boldsymbol{A}}_1 + j\vec{\boldsymbol{A}}_2$, which should be *directly* substituted into the CEM software package. This provides a concise description of this model.

Step 5. *Testing the ideal-coil concept: accuracy within unloaded coil*. An unloaded (without the body) coil shown in **Figure 3.9** with 16 rungs, 32 matching capacitors (each of which can be connected to a driving port), with the diameter of 604 mm and the length of 650 mm. All relevant simulations are performed at 63.87 MHz ($B_0 = 1.5$ T) using ANSYS Electronics Desktop (ANSYS HFSS) v.16.2, Perfectly Matched Layer (PML) terminations, and 12 adaptive mesh refinement passes.

A comparison will be made with an accurate practical solution [16], which uses the circuit co-simulator to drive the coil with *two ports* spaced by 90° (ports 1 and 5) and also establishes the port-matching networks. This solution reports the value of $C_0 = 106.2$ pF, while this proposed method reports $C_0 = 106.23$ pF for one resonant mode and $C_0 = 106.16$ pF for another mode. The agreement is almost exact! The corresponding distributions of the magnitude of magnetic field $\boldsymbol{B}_1^+$ within the shielded coil at the coil center are shown in **Figure 3.12 b, c** given the *same* input power of 1 W and the *same* color scale. Both solutions are very close to each other, although the proposed solution generates slightly more symmetric and homogeneous field, since *all ports* are now driven as appropriate.

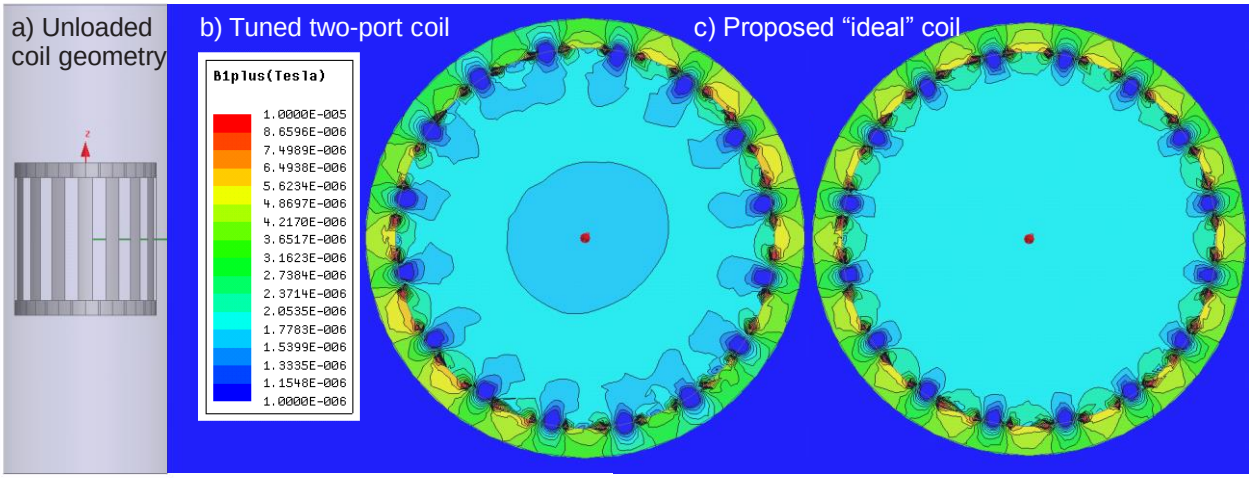

Figure 3.12 Magnetic field distribution within the unloaded RF coil at 1 W input power. a) – Coil geometry; b) – practical solution with two matched driving ports; c) – The proposed ideal model with all matched driving ports. The same color scale is used on both figures.

Step 6. *Testing the ideal-coil concept: accuracy within the loaded coil*. This method is applied to compute the circularly-polarized magnetic field $\boldsymbol{B}_1^+$ in an ideally matched/tuned coil *loaded* with the VHP-Female. **Figure 3.13** shows preliminary simulations with the VHP-Female model for the magnitude distributions of the magnetic field $\boldsymbol{B}_1^+$ within the shielded coil in a transverse plane passing through the coil center. The same parameters as in **Figure 3.12** are used but the color scale is different. All relevant simulations are performed using ANSYS Electronics Desktop (ANSYS HFSS) v.16.2, PML terminations, and 3 adaptive mesh refinement passes.

The loaded (with the body) coil shown in **Figure 3.9** with 16 rungs, 32 matching capacitors (each of which can be connected to a driving port), with the diameter of 640 mm and the length of 689 mm ***at the head landmark*** (the center of the coil coincides with the top of the cerebellum).

A comparison is again made with the accurate practical solution [16], which uses the circuit co-simulator to drive the coil with *two ports* spaced by 90° (ports 1 and 5) and also establishes the port-matching networks.

Although this is a rather complicated case for coil tuning since the coil is loaded highly asymmetrically, both solutions again predict quite similar magnetic field magnitudes. This generic solution generates a slightly more symmetric and homogeneous field.

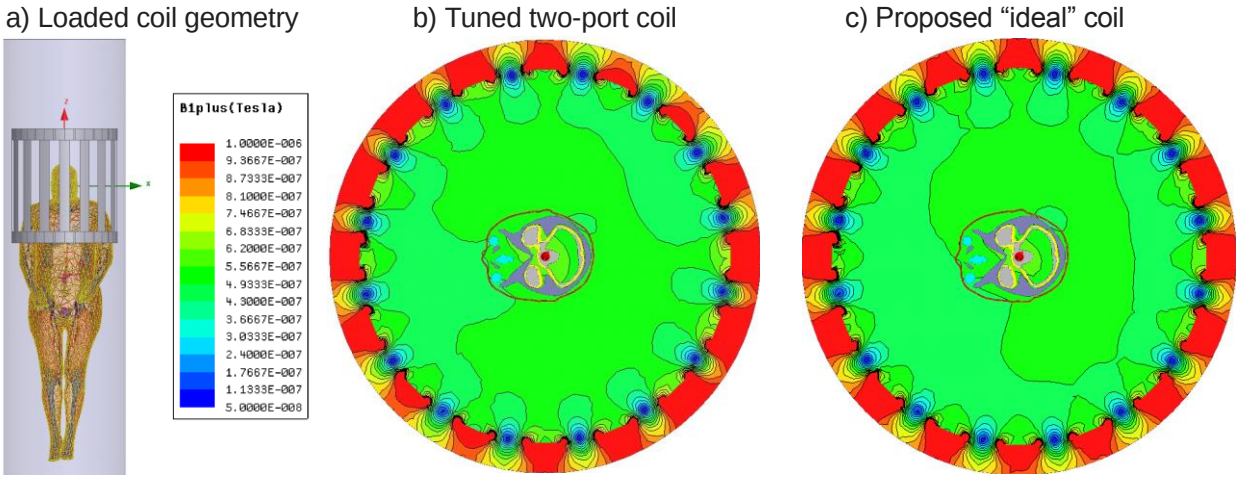

Figure 3.13 Magnetic field distribution within the RF coil loaded with the VHP-Female v.3.0 model at 1 W input power. a) – Landmark of the model inside the birdcage b) – practical solution with two matched driving ports; c) – our ideal model with all matched driving ports. The same color scale is

Step 7.*Testing the ideal-coil concept: accuracy for SAR computations at the head landmark*. This method is applied to compute *SAR* in an ideally matched/tuned coil *loaded* with the VHP-Female model. **Figure 3.15** shows preliminary simulations for the distributions of the local non-averaged *SAR* within the shielded coil at the coil center for the VHP-Female model. The same coil, parameters and the landmark as in **Figure 3.14** are used. All relevant simulations are performed using ANSYS Electronics Desktop (ANSYS HFSS) v.16.2, PML terminations, and 3 adaptive mesh refinement passes.

A comparison is again made with the accurate practical solution [16], which uses the circuit-co-simulator to drive the coil with *two ports* spaced by 90° (ports 1 and 5) and establishes the port-matching networks.

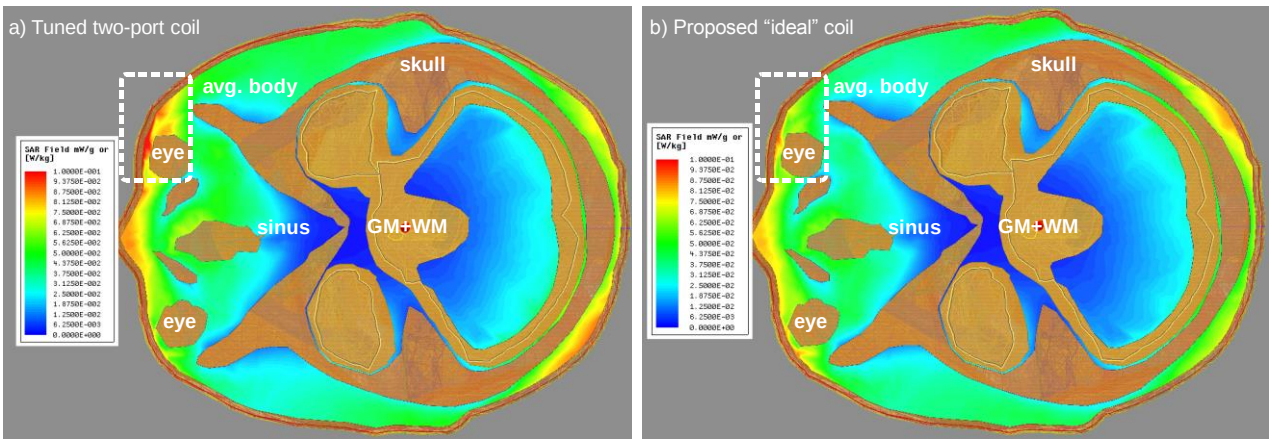

Figure 3.14 SAR distribution in the cranium within the RF coil loaded with the VHP-Female v.3.0 model at 1 W input power. a) – Practical solution with two matched driving ports; b) –The ideal model with all matched driving ports. The same color scale is used on both figures. Shown are the SAR values in the cortical transverse plane, the fields in the cerebellum object and in the "average body" object.

Both solutions generate similar *SAR* distributions. At the same time, this generic solution shown in **Figure 3.14b** generates a smoother and likely *more realistic SAR* specifically near the right eye. The corresponding local *SAR* maximum may be caused by an insufficient quality of the local FEM mesh or by other reasons.

Based on the developed workflow, the *SAR* distributions has been established in transverse, coronal, and sagittal planes, and compare those distributions with the "standard" margins described next.

Step 8.*Testing the ideal-coil concept: accuracy for SAR computations at the shoulder landmark.* As a final example, **Figure 3.15** illustrates the *SAR* distribution in a birdcage coil at the shoulder landmark for the VHP-Female virtual human. All relevant simulations are performed using ANSYS Electronics Desktop (ANSYS HFSS) v.16.2, PML terminations, and 3 adaptive mesh refinement passes. The loaded (with the body) coil shown in **Figure 3.9** with 16 rungs, 32 matching capacitors (each of which can be connected to a driving port), with the diameter of 640 mm and the length of 689 mm at the ***shoulder landmark*** (the center of the coil coincides with the top of vertebra # T7).

The accurate practical solution, which uses the circuit-co-simulator to drive the coil with *two ports* spaced by 90° (ports 1 and 5) [16] and the ideal-coil solution shown in **Figure 3.15** are virtually identical!

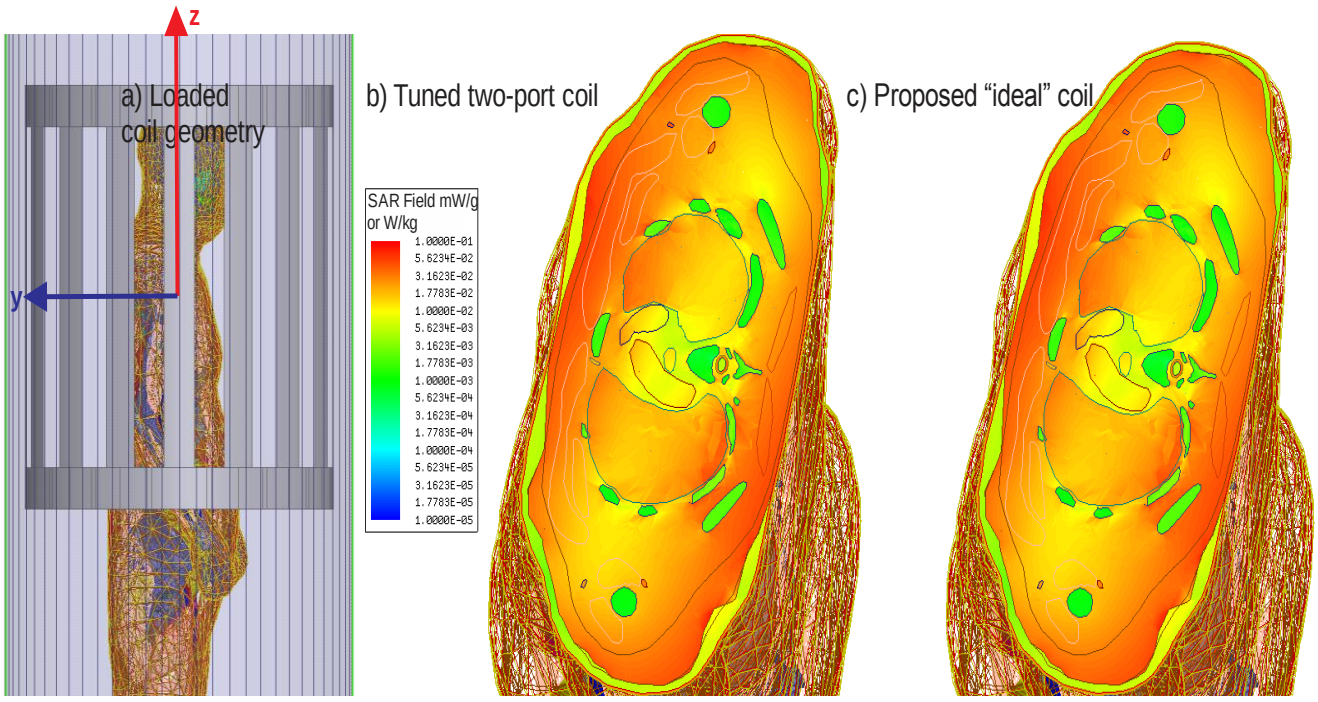

Figure 3.15 SAR distribution for a coil loaded with the VHP-Female v.3.0 model at 1 W input power. a) – Landmark of model inside the birdcage; b) – practical solution with two matched driving ports; c) – Ideal model with all matched driving ports. The same color scale is used on both figures. The two solutions are virtually identical when the commonly accepted logarithmic scale is used.

In summary, the generic method for testing the "quality" of virtual humans in the MR imaging coil has the following advantages:

1. No need for a circuit co-simulator and coupling procedure of the co-simulator with the chief CEM full-wave computational software. According to historic and anecdotal sources, such a coupling is a non-trivial technical task even for highly-skilled professionals. This is especially important for the users of those software packages which simply do not have a supplementary circuit co-simulator. Cases in point are Abaqus, COMSOL, WIPL-D, and Empire-XPU.
2. Independence on the particular number of driving ports of the RF coil. *Any* RF coil topology can be considered, which makes the method widely applicable.
3. Good agreement with accurate practical solutions as evidenced by **Figures 3.12**, **3.13**, **3.14,** and **3.15**.
4. Simplicity as compared to other coil tuning methods [16]-[23]. The entire technical approach described above will be realized as a MATLAB script.
5. Rapid result generation.

3.5.2 Establish Margins for $\boldsymbol{SAR}$ Variations Based on the Workflow for testing the "quality" of the VHP-Female Model with an Ideal Coil and Other Literature Sources

3.5.2.1 Definitions

The local SAR (W/kg) is defined through averaging the dissipated power per unit mass over a small (ideally infinitesimally small) volume V, that is

$$SAR(\boldsymbol{r}) = \frac{1}{V}\int_{\boldsymbol{V}} \frac{\sigma(\boldsymbol{r})}{2\rho(\boldsymbol{r})}|\boldsymbol{E}(\boldsymbol{r})|^2 dV \tag{5}$$

Here, $\sigma(\boldsymbol{r})$ is the local tissue conductivity, $\rho(\boldsymbol{r})$ is the local mass density, and $|\boldsymbol{E}(\boldsymbol{r})|$ is the electric field magnitude at an observation point. The body-averaged or the whole-body SAR_{body} is given by averaging over the entire body volume, as

$$SAR_{body} = \frac{1}{V_{body}}\int_{V_{body}} \frac{\sigma(\boldsymbol{r})}{2\rho(\boldsymbol{r})}|\boldsymbol{E}(\boldsymbol{r})|^2 dV \tag{6}$$

Similarly, SAR_{1g} is given by averaging over a volume with the weight of 1 g

$$SAR_{1g}(\boldsymbol{r}) = \frac{1}{V_{1g}}\int_{V_{1g}} \frac{\sigma(\boldsymbol{r})}{2\rho(\boldsymbol{r})}|\boldsymbol{E}(\boldsymbol{r})|^2 dV \tag{7}$$

$SAR_{10g}(\boldsymbol{r})$ is found in the similar fashion.

3.5.2.2 Method

[1] Consider the loaded (with the VHP-Female v.3.0 model, 88 kg) whole-body coil shown in **Figure 3.9** with 16 rungs, 32 matching capacitors (each of which can be connected to a driving port), with the diameter of 640 mm and the length of 689 mm, which is close to the dimensions given in Ref. [31].

[2] Set the coil at the ***shoulder landmark*** (the center of the coil coincides with the top of vertebra # T7).

[3] Also consider the coil at ***abdominal landmark*** (the center of the coil coincides with the top of vertebra # L1).

[4] All relevant simulations are performed using ANSYS Electronics Desktop (ANSYS HFSS) v.16.2 including PML terminations. All relevant simulations are performed at 63.87 MHz ($B_0 = 1.5$ T). For every case, we will generate solutions ***with 1 adaptive mesh refinement pass (about 0.5 M tetrahedra) and 8 adaptive mesh refinement passes (about 2.0 M tetrahedra)***, respectively.

[5] For every case, the ***model of the ideal perfectly-matched coil*** driven at all ports described above and with 1 W of total input power is used. ***For each particular number of passes (1, 8, etc.), the coil must be retuned as described above once the solution is complete. Only after that, the correct fields solutions can be obtained.***

[6] Then ***normalize the fields solutions*** given the desired magnitude of $\boldsymbol{B}_1^+$ at the coil center of 1 μT. The normalization is done in the form

$$SAR = \frac{SAR}{(\boldsymbol{B}_1^+/1\mu T)^2} \tag{8}$$

[7] For every case, output the local SAR computed in ANSYS Electronics Desktop to MATLAB over a uniform 3D grid of ***2 mm in size***. The corresponding ASCII file size is approximately 1 Gbyte.

[8] Compute the whole-body SAR_{body} from this data according to Eq. (6) directly in MATLAB. This step is trivial.

[9] Compute SAR_{1g} by ***finding a volume surrounding the observation point and having the mass of exactly 1 g, and then performing averaging according to Eq. (7)***. All operations will be performed in MATLAB using parallel computing with 16-24 workers. This averaging volume will contain approximately 125 individual voxels (2×2×2 mm each) ***closest to the observation point***. The observation points form a 3D sub-grid spaced of 20 mm and 10 mm, respectively. Processing finer grids would require running times in excess of 48 hours.

[10] The tissue density will be set at 1 g/cm^3 uniformly in space.

[11] Alternatively, extract the density data from the ANSYS voxel data on the 2 mm master voxel grid by computing both local SAR and local PLD and then performing SAR computations more accurately. The difference between the two approaches is found to be within 10% everywhere except the bone volume.

[12] Compute SAR_{10g} in the same way. In this case, the averaging volume will contain approximately 1250 individual voxels (2×2×2 mm each) ***closest to the observation point***.

By analyzing **Figure 3.16,** note

A. The accurate solution with eight adaptive mesh refinement passes generates a more realistic SAR distribution. In particular, two non-physical maxima of the SAR observed at the top of the head are no longer present.
B. The accurate solution with eight adaptive mesh refinement passes and the coarse solution with one adaptive pass generate approximately ***the same SAR distributions*** despite or rather thanks to the fact that the coil has been retuned separately in both cases case.
C. The maximum SAR for the present landmark is observed in the upper shoulder/neck area and in the arms area.
D. A gap between the arms and the body may generate large SAR values.

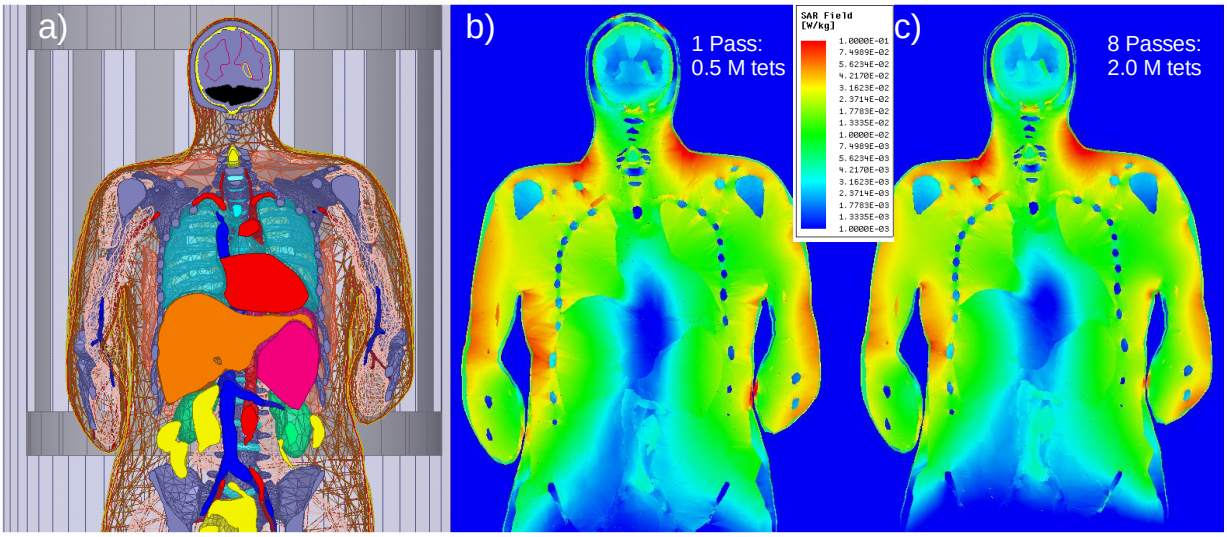

Figure 3.16 Local SAR distribution for a coil loaded with the VHP-Female v. 3.0 model at 1 W input power in the coronal plane at 63.87 MHz. a) – Landmark of model inside the birdcage; b) – solution with one adaptive pass; c) – solution with eight adaptive passes.

3.5.2.3 Results

The SAR values have been analyzed previously in Refs. [24]-[32] and in other reference sources. Table 3.1 given below compares the VHP-Female results, results of Refs. [25],[29],[30], and [31], and other literature data. We use a 10 mm sub-grid for accurate computations of $SAR_{1g}(\boldsymbol{r})$ and $SAR_{10g}(\boldsymbol{r})$.

Table 3.1. Computed SAR values from different sources (W/kg) given 1 μT $\boldsymbol{B}_1^+$ field (at the coil isocenter or averaged).

Entity/Country	**Model Name**	**Method**	**Coil landmark**	**Whole-body *SAR***	**Max. non-averaged local *SAR***	**Max. 1g local *SAR***	**Max. 10g local *SAR***
NEVA EM LLC, USA	VHP-Female	FEM 1Pass 64 MHz	Shoulder/ heart (top of vert. T7)	0.16	44.5	5.22	2.61
NEVA EM LLC, USA	VHP-Female	FEM 8Passes 64 MHz	Shoulder/ heart (top of vert. T7)	0.13	11.8	3.00	1.24
Penn State USA	Vis. Human Female	FDTD Voxel size unknown 64 MHz	Heart	Normal to 0.15	NA	NA	3.35
Karlsruhe Inst. of Techn. Germany	Vis. Human Male	FDTD 5mm Voxel 128 MHz	Abdominal	0.58	22.78	11.90	8.79
NEVA EM LLC, USA	VHP-Female	FEM 1Pass 128 MHz	Abdominal	0.20	43.8	7.29	3.25

Entity/Country	Model Name	Method	Coil landmark	Whole-body *SAR*	Max. non-averaged local *SAR*	Max. 1g local *SAR*	Max. 10g local *SAR*
IT'IS Foundation, Switzerland	Nagaoka Female	FDTD 2 mm Voxel 64 MHz	Abdominal	0.13	NA	3.2	2.1
Karlsruhe Inst. of Techn. Germany	Vis. Human Male	FDTD 3.5mmVoxel 128 MHz	Abdominal	0.57	24.91	11.63	6.98
Karlsruhe Inst. of Techn. Germany	Vis. Human Male	FDTD 2.5mmVoxel 128 MHz	Abdominal	0.54	35.68	13.76	8.88
IT'IS Foundation, Switzerland	Nagaoka's Female	FDTD 2mm Voxel 128 MHz	Abdominal	0.24	NA	5.3	3.9
IT'IS Foundation, Switzerland	Vis. Human Male	FDTD 2mm Voxel 128 MHz	Abdominal	0.31	NA	5.2	3.9
IT'IS Foundation, Switzerland	Vis. Human Female	FDTD 3.0mmVoxel 128 MHz	Heart	Normal. to 0.15	NA	2.46-4.11 Varies	1.23-2.03 Varies
IT'IS Foundation, Switzerland	Vis. Human Male	FDTD 3 mm Voxel	Pelvic	Normal. to 0.54	NA	8.91-14.8 Varies	4.21-6.86 Varies

3.5.2.4 Discussion – first observation

One principal observation which follows from Table 3.1 is that the non-averaged local SAR and $\max(SAR_{1g}(\boldsymbol{r}))$ decrease (or equivalently converge) when applying the FEM to the CAD model with adaptive mesh refinement and a larger number of mesh refinement steps while the whole-body SAR remains nearly the same. The evidence is given by second and third rows of Table 3.1.

This is in sharp contrast to the FDTD method and the voxel models where the non-averaged local SAR and $\max(SAR_{1g}(\boldsymbol{r}))$ generally increase (or equivalently diverge) when refining the voxel grid while the whole-body SAR still remains nearly the same. The evidence is given by fourth, fifth, and sixth rows of Table 3.1.

Indeed, a part of this advantage is due the fact that the final voxelization of the FEM data for SAR computations in this report assumes the voxel size of 2 mm. However, given that the size of an average FEM tetrahedron even after eight mesh refinement adaptive passes significantly exceeds 2 mm, the general advantage of the FEM approach with adaptive mesh refinement becomes evident.

The FDTD method could probably be modified to work equally well when a sub-gridding technique [33],[34] is used.

3.5.2.5 Discussion – second observation

SAR results for the shoulder/heart landmark are in a full agreement with the known literature data when an accurate solution with eight adaptive mesh refinement passes and a final mesh containing ~ 2M tetrahedra is used. This is evidenced by the results reported in Table 3.1. Since the SAR data vary widely, we may establish the following margins (all data in W/kg) for

[1]. the heart, shoulder, abdominal, and pelvic landmarks;
[2]. different human models;
[3]. different RF coli types, and for 1.5 T and 3 T fields

based on Table 3.1 and other sources:

$$0.13 < SAR_{body} < 0.54 \text{ for 1 } \mu\text{T field} \tag{9}$$

$$2.46 < max\left(SAR_{1g}(\boldsymbol{r})\right) < 14.8 \text{ for 1 } \mu\text{T field} \tag{10}$$

$$1.23 < max\left(SAR_{10g}(\boldsymbol{r})\right) < 8.88 \text{ for 1 } \mu\text{T field} \tag{11}$$

3.5.3 A Generic Algorithm for Testing a Virtual Human $\boldsymbol{SAR}$

1. A fully parameterized standard high-pass birdcage coil model with 16 rungs, 32 matching capacitances (any of which can be connected to a port) shown in Fig. 3.9. The base coil will have the diameter of 640 mm and the length of 690 mm. These dimensions are in agreement with the most common literature data [31] and with our data. The model is available in a number of common formats: STL, STEP, MATLAB, and SolidWorks. Thus, it can be imported to any CEM software. A shielding open cylinder will be provided as well.

2. A virtual human has been tested at two landmarks: heart (center of the coil coincides with the top of vertebra T7) and abdominal (center of the coil coincides with the top of vertebra L1) and at two frequencies: 64 MHz (1.5 T) and 128 MHz (3.0 T).

3. A CEM package computes the data following the ideal perfectly-tuned or "universal" coil model described on the previous sections. Namely, all capacitances are replaced by active ports with a port impedance of 50 Ω. As a result, the system scattering matrix $\widehat{\boldsymbol{S}}$, system impedance matrix $\widehat{\boldsymbol{Z}}$, and system admittance matrix $\widehat{\boldsymbol{Y}}$ will be obtained. This operation is standard for any commercial CEM software.

4. A short generic MATLAB script has been written which, given these three matrices (in reality, only one is necessary), computes the required sources (wattage and phase) for all 32 ports normalized to 1 W of total input power. This script is given in Appendix A. These sources need to be substituted into the CEM package.

5. First, the users' workflow will be tested for the unloaded coil by outputting the $\boldsymbol{B}_1^+$ field at the coil center at 64 MHz and 128 MHz, respectively. These two particular values are obtained via accurate ANSYS Electronics Desktop modeling. A loaded coil can be modeled only if an agreement is established.

6. Next, the coil is set at the two positions described above and simulations performed at two frequencies (64 MHz and 128 MHz). This operation results in four separate projects.

7. After the project completes, steps 3 and 4 need to be performed. As a result, the local SAR distribution is obtained and the $\boldsymbol{B}_1^+$ field at the coil center.

8. The local SAR distribution is normalized to 1 μT $\boldsymbol{B}_1^+$ field at the coil center following Eq. (8).

9. Finally, three parameters: SAR_{body}, $max\left(SAR_{1g}(\boldsymbol{r})\right)$, and $max\left(SAR_{10g}(\boldsymbol{r})\right)$ are be computed either following users' own approach or using the MATLAB script.

10. This gives a set with total 12 representative SAR values to be compared with Eqs. (9), (10), (11) or their modifications. Since these values are within the margins, the model passes and can be validated.

References

[1]. Nazarian, A., J. Yanamadala, G. Noetscher, M. W. Piazza, S. Louie, A. Prokop, and S. N. Makarov, "Applications of Virtual Humans in Medical Research: VHP-Female CAD Model," IEEE Antennas & Propagation Magazine, 2016, under review.

[2]. Makarov, S. and G.M. Noetscher, "Human Models for Wireless Communication and Cyber Physical Systems," Invited Tutorial, IEEE GLOBECOM 2016, Dec. 4-8 2016 Washington, DC. Online: http://globecom2016.ieee-globecom.org/program/industry-program/ife-tutorials

[3]. Makarov S., J. Yanamadala, M. Piazza, A. Helderman, N. Thang, E. Burnham, A. Pascual-Leone, "Preliminary Upper Estimate of Peak Currents in Transcranial Magnetic Stimulation at Distant Locations from a TMS Coil,"IEEE Transactions on Biomedical Engineering, vol. 63, no. 9, pp. 1944-1955, Sep. 2016. PMID: 26685221

[4]. Tran, A. L., G. Noetscher, S. Louie, A. Prokop, A. Nazarian, and S. N. Makarov, "FEM Human Body Model with Embedded Respiratory Cycles for Antenna and E&M Simulations," 40th 2016 Antennas Appl. Sym., Monticello, IL, Sep. 20-22 2016.

[5]. Tankaria, H., X.J. Jackson, R. Borwankar, G.N.K. Srichandhru, A.L. Tran, J. Yanamadala,G. M. Noetscher, A. Nazarian, S. Louie, and S.N. Makarov, "VHP-Female Full-Body Human CAD Model for Cross-Platform FEM Simulations – Recent Development and Validations," 38th Annual Int. Conf. of the IEEE Engineering in Medicine and Biology Society (EMBC 2016), Orlando, FL, Aug. 16-20 2016.

[6]. Tankaria, H., X.J. Jackson, R. Borwankar, G.N.K. Srichandhru, A.L. Tran, J. Yanamadala, S.N. Makarov, and A. Pascual-Leone, "Full-Body FEM Pregnant Woman Model and Applications," 38th Annual Int. Conf. of the IEEE Engineering in Medicine and Biology Society (EMBC 2016), Orlando, FL, Aug. 16-20 2016.

[7]. Noetscher, G.M., M. Horner, S. Louie, D.S. Quinn, S.N. Makarov, "Modification of ANSYS Male Computational CAD Model and Resulting FEM Performance," 38th Annual Int. Conf. of the IEEE Engineering in Medicine and Biology Society (EMBC 2016), Orlando, FL, Aug. 16-20 2016.

[8]. Noetscher, G.M., J. Yanamadala, H.V. Tankaria, X. J. Jackson, S. Louie, A. Prokop, A. Nazarian, and S. Makarov, "VHP-Female CAD Human Model Family for Antenna Modeling, "2016 IEEE International Symposium on Antennas and Propagation/USNC-URSI National Radio Science Meeting, June 26, 2016.

[9]. Yanamadala, J., G.M. Noetscher, S. Louie, A. Prokop, M. Kozlov, A. Nazarian, and S. N. Makarov, "Multi-Purpose VHP-Female Version 3.0 Cross-Platform Computational Human Model," 10th European Conference on Antennas and Propagation 2016 (EuCAP16), Davos, Switzerland, April 10-15 2016.

[10]. Noetscher G.M., J. Yanamadala, S. Louie, A. Nazaian, and S. N. Makarov, "Computational Human Model VHP-Female Derived from Datasets of the National Library of Medicine," IEEE Pulse Magazine April 2016. Online:http://pulse.embs.org/march-2016/creating-a-computational-human-model/

[11]. Noetscher, G., S. Louie, and S. Makarov, "Modern Full Body Human CAD Models for Microwave Simulations," Inivited Tutorial, 10th International Symposium on Medical Information and Communication Technology (ISMICT'16), Worcester, MA, March 20-23, 2016 Online: http://www.cwins.wpi.edu/ismict16/Advanced%20Program.pdf
[12]. Noetscher, G.M., J. Yanamadala, M. Kozlov, S. Louie, A. Nazarian, and S. Makarov, "VHP-Female v3.0 FEM/BEM Computational Human Phantom,"24thInternational Meshing Roundtable (IMR24), Austin, TX, Oct. 12-15, 2015.
[13]. Yanamadala, J., G. Noetscher, M. Piazza, A. Helderman, N. Thang, T. Dolma, T. Trinh, J. Zhang, M. Islam, S. Xie, V. Rathi, S. Maliye, H. Win, A. Tran, X. Jackson, P. Carberry, A. Htet, M. Kozlov, S. Louie, A. Nazarian, S. Makarov, "VHP-Female v. 2.0 Full-Body Computational Phantom: ANSYS HFSS Performance Metrics in Application to Antenna Radiation and Scattering," 39th 2015 Antenna Applications Symposium, Monticello, IL, Sep. 22-24, 2015, pp. 453-461.
[14]. Yanamadala, J., G. M. Noetscher, V. K. Rathi, S. Maliye, H. A. Win, A. L. Tran, X. J. Jackson, A. T. Htet, M. Kozlov, A. Nazarian, S. Louie, and S. N. Makarov, "New VHP-Female v. 2.0 Full-Body Computational Phantom and Its Performance Metrics Using FEM Simulator ANSYS HFSS," 37th Annual Int. Conf. of the IEEE Engineering in Medicine and Biology Society, Milano, Italy, pp.3237-3241, 25-29 Aug. 2015. PMID: 26736982.
[15]. Kozlov, M., G. M. Noetscher, A. Nazarian, S.N. Makarov, "Comparative analysis of different hip implants within a realistic human model located inside a 1.5T MRI whole body RF coil," 37th Annual Int. Conf. of the IEEE Engineering in Medicine and Biology Society, Milano, Italy, pp.7913-7916, 25-29 Aug. 2015. PMID: 26738127.
[16]. Lemdiasov R, Obi A, Ludwig R. A Numerical Postprocessing Procedure for Analyzing Radio Frequency MRI Coils. Concepts in Magnetic Resonance Part A. 2011; 38A(4): 133–147.
[17]. Kozlov M, Turner R. Fast MRI coil analysis based on 3-D electromagnetic and RF circuit co-simulation. J Magn Reson. 2009; 200: 147–152.
[18]. Kozlov M, Turner R. A comparison of Ansoft HFSS and CST Microwave Studio simulation software for multi-channel coil design and SAR estimation at 7 T MRI. PIERS Online. 2010; 4: 395–399.
[19]. Roemer PB, Edelstein WA, Hayes CE, Souza SP, Mueller OM. The NMR phased array. Magn Reson Med. 1990; 16: 192–225.
[20]. Chen J, Feng Z, Jin J-M. Numerical simulation of SAR and B1-field inhomogeneity of shielded RF coils loaded with the human head. IEEE Trans Biomed Eng. 1998; 45: 650–659.
[21]. Jiao D, Jin J-M. Fast frequency-sweep analysis of RF coils for MRI. IEEE Trans Biomed Eng. 1999; 46: 1387–1390.
[22]. Reza S, Vijayakumar S, Limkeman M, Huang F, Saylor C. SAR simulation and the effect of mode coupling in a birdcage resonator. Conc Magn Reson Part B: Magn Reson Eng. 2007; 31: 133–139.

[23]. Ibrahim TS, Lee R, Baertlein BA, Abduljalil AM, Zhu H, Robitaille P-ML. Effect of RF coil excitation on field inhomogeneity at ultra high fields: a field optimized TEM resonator. Magn Reson Imaging. 2001; 19: 1339–1347.
[24]. Oh S, Webb AG, Neuberger T, Park B, Collins CM. Experimental and numerical assessment of MRI-induced temperature change and SAR distributions in phantoms and in vivo. Magn Reson Med. January 2010; 63(1): 218-23. PMCID: PMC2836721.
[25]. Homann H. SAR Prediction and SAR Management for Parallel Transmit MRI. Karlsruhe Translations on Biomedical Eng. 2012; 16: 1-124.
[26]. Collins CM, Li S, Smith MB. SAR and B1 Field Distribution in a Heterogeneous Human Head Model with a Birdcage Coil. Magnetic Resonance in Medicine. 2005; 40(6): 847-856.
[27]. Rennings A, Chen L, Otto S, Erni D. B1-Field Inhomogeneity Problem of MRI: Basic Investigation on a Head- Tissue-Simulating Cylinder Phantom Excited by a Birdcage-Mode. 42nd European Microwave Conference, The Netherlands, Amsterdam, 2012 November 1; pp. 542-545.
[28]. Tomas BP, Li H, Anjum MR. Design and Simulation of a Birdcage Coil using CST Studio Suite for Application at 7T. IOP Conference Series: Materials Science and Engineering. 2013 February 1; 51(1):1-6.
[29]. Yeo DTB, Wang Z, Loew W, Volgel MW, Hancu I. Local SAR in High Pass Birdcage and TEM Body Coils for Multiple Human Body Models in Clinical Landmark Positions at 3T. Journal of Magnetic Resonance Imaging. 2011 May; 33(5): 1209 – 1217. PMCID: PMC3081105.
[30]. Liu W, Collins CM, Smith MB. Calculation of B1 Distribution, SAR, and SNR for a Body-size Birdcage Coil Loaded with Different Human Subjects at 64 and 128 MHz. Applied Magnetic Resonance, 2005 March; 29(1): 5-18. PMID:23565039 PMCID: PMC3615460.
[31]. Cabot E, Christ A, Kuster N. Whole Body and Local SAR in Anatomical Phantoms Exposed to RF Fields from Birdcage Coils. Proceedings of the 29th General Assembly of the International Union of Radio Science. 2008 August 7-16. Chicago, USA.;
[32]. Kozlov M, Turner R. RF Transmit Performance Comparison for Several MRI Head Arrays at 300 MHz. Progress in Electromagnetic Research Symposium Proceedings. 2013 March 28 Taipei: 1052-1056.
[33]. Kozlov M, Bazin PL, Möller HE, Weiskopf N. Influence of Cerebrospinal Fluid on Specific Absorption Rate Generated by 300 MHz MRI Transmit Array. 10th European Conference on Antennas and Propagation (EuCAP). 2016 April. Davos. Switzerland. pp. 1-5.
[34]. Taflove A. Computational Electrodynamics, The Finite Difference Time Domain Approach, Third Ed., Artech House, Norwood, MA, 2005.
[35]. Thoma P, Weiland, T. A consistent subgridding scheme for the finite difference time domain method," Int. J. of Numerical Modelling, vol. 9, pp. 359-374, 1996.

Chapter 4

Application: Novel approach towards non-ionizing technique for osteoporosis detection

4.1 Introduction

Osteoporosis is a medical condition where the loss of bone tissue makes the affected bone brittle and fragile. [6] Osteoporosis progresses over time. The osteoporotic bone is fragile, porous, and easy to break. The disease is more common among women and older adults. A patient suffering from osteoporosis is prone to bone fracture and injuries. The general observation is such that osteoporosis affects skinny, and old females.

This chapter introduces a novel diagnostic procedure and suggests a non-ionizing approach towards the detection of osteoporosis. The VHP-Female model was used to optimize and test the reader patch antenna in ANSYS HFSS.

The optimized physical parameters were used to construct a prototype testbed for proof of concept.

4.1.1 Available procedures for Osteoporosis detection

Figure 4.1 shows the normal and osteoporotic bone. It is clearly visible from the image that the density of the osteoporotic bone is much less as compared to the normal bone. The clinical procedure involves a test described as the bone density scan.

This test measures bone mineral density (BMD) by the amount of x-rays absorbed by tissue and bone. This procedure is performed in the Dual-energy X-ray absorptiometry (DXA) machine.

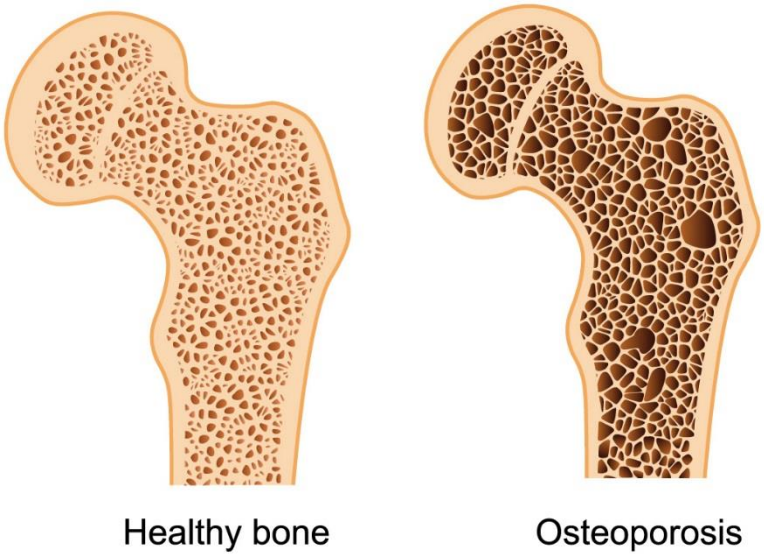

Figure 4.1 General representation of a healthy and osteoporotic bone.[7]

The DXA machine converts raw density information to a T score and Z score. The T score measures the amount of bone you have in comparison to a normal population of younger people and is used to estimate your risk of developing a fracture. The Z score measures the amount of bone you have in comparison to those in your age group. This number can help indicate whether there is a need for further medical tests.

4.1.2 Requirement for better solution

We very well know the harmful effects of ionizing radiation. This radiations can damage the DNA inside living cells in the following two ways. First, radiation can strike the DNA molecule directly, ionizing and damaging it. Second, radiation can ionize water molecules, producing free radicals that react with and damage DNA molecules.

Once the atoms in the living cells become ionized one of the three things usually happens – the cell dies, the cell repairs itself, or the cell mutates incorrectly and can become cancerous. Different cells are affected differently by ionizing radiation. When we consider the effects of radiation on specifically the bone, it is observed that the bone health is affected significantly. This has fueled research in exploring non-ionizing radiations for detecting the bone health.

4.2 Background for the novel approach

Microwave imaging of (heel) bone was *first* introduced by the group of Dr. K. D. Paulsen at Dartmouth about six years ago with the idea of its potential application as an alternative non-ionizing diagnostic method of bone health [1] -[5]. Due to the well-known complexity and poor spatial resolution of the standard microwave imaging setup used in these studies, no clinically applicable results have been generated to date. However, the underlying physical idea of this method is, in our opinion, simple and powerful. In osteoporosis, bone mass decreases and pore size increases. The lost bone mass is replaced by a mixture of yellow bone marrow (with a dielectric constant that is *five times less* than the value for normal trabecular bone at 900 MHz) and fat (with a dielectric constant is *two times less* than the value for normal trabecular bone at 900 MHz). Such a drastic decrease in the dielectric constant must generate significantly stronger scattering and/or reflection of an RF signal passing through the bone. In principle, we only need to track a power ratio of such a signal along the path through the bone instead of restoring the complete permittivity map of the bone and the surrounding tissues, as initially attempted in [1]-[5].

The figure below shows difference in the material properties of the healthy bone and the osteoporotic bone. The data has been extracted from the IT'IS database.

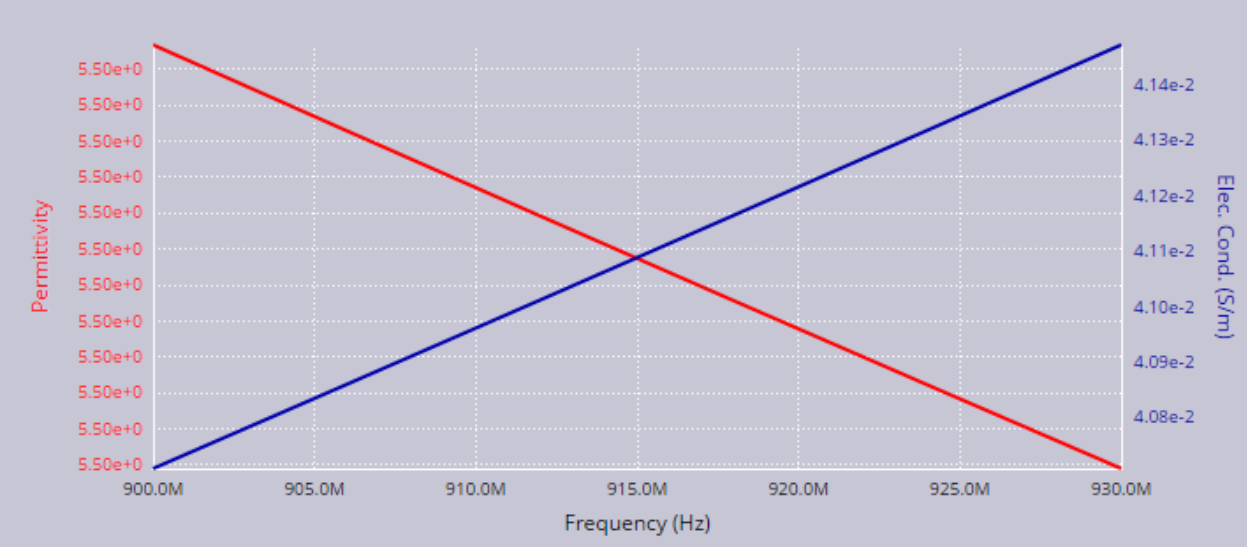

Figure 4.2 Electric Conductivity and permittivity for yellow bone marrow (osteoporotic bone tissue) at 915 MHz

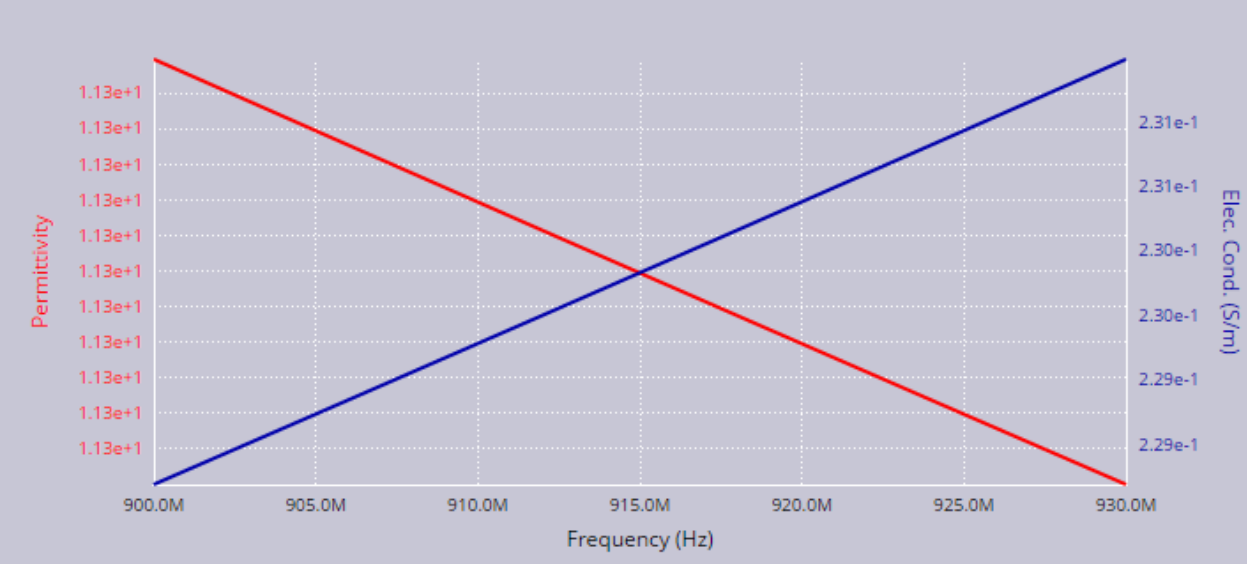

Figure 4.3 Electric Conductivity and permittivity for red bone marrow (healthy bone tissue) at 915 MHz

Consider applying a completely different technical approach. Instead of a typical microwave imaging setup, using a modern RFID reader at 900 MHz with an on-skin reader (pumping) antenna and a number of on-skin passive RFID tags surrounding the bone in the form of an array. Given that the reader outputs RSSI (Received Signal Strength Indicator) from every tag every 0.1 s, this setup will eliminate the need for a custom beamforming network and will reduce both the cost and the complexity by an order of magnitude.

4.3 EM Background

A cortical bone shell with trabecular bone matter inside is a scatterer of the electromagnetic signal since the dielectric contrast (ratio of the respective dielectric constants) with the surrounding muscle tissue (or average body tissue) is significant. The dielectric contrast defines the degree of scattering/reflection of an electromagnetic signal at the boundary between two dielectric tissues: the larger the contrast, the stronger the signal loss. In the extreme osteoporotic case, the entire trabecular bone volume is replaced by a mixture of yellow bone marrow and fat, which leads to a much larger average dielectric contrast (about 5-6 vs. 2.8) between the bone and the surrounding tissue. In the general case, measured dielectric constant values for trabecular bone matter with bone loss may vary. On-skin RFID tags should be quite sensitive to this change since the signal travels twice through the bone (from the reader to the tag and vice versa) and gets scattered significantly stronger when the average dielectric contrast increases.

From the viewpoint of numerical modeling (ANSYS HFSS), the scattered signal from an *i*-th tag antenna S_i at the reader is computed by finding the total complex reflection coefficient of the reader antenna port twice: as S_{i1} when the *i*-th tag chip is at low chip impedance or powered ($Z_c = 20 - j200\ \Omega$) and as S_{i0} when the *i*-th tag is at high chip impedance ($Z_c \geq 10$ kΩ).The difference,

$$S_i = S_{i1} - S_{i0} \tag{12}$$

the scattered signal from the *i*-th tag at the reader port. Its power in dB, $10\log_{10}|S_i|^2$, is the RSSI of the *i*-th tag. All other chips in the array should have a high chip impedance (open).

Figure 4.4 shows one of the many HFSS project constructed to optimize the patch antenna performance.

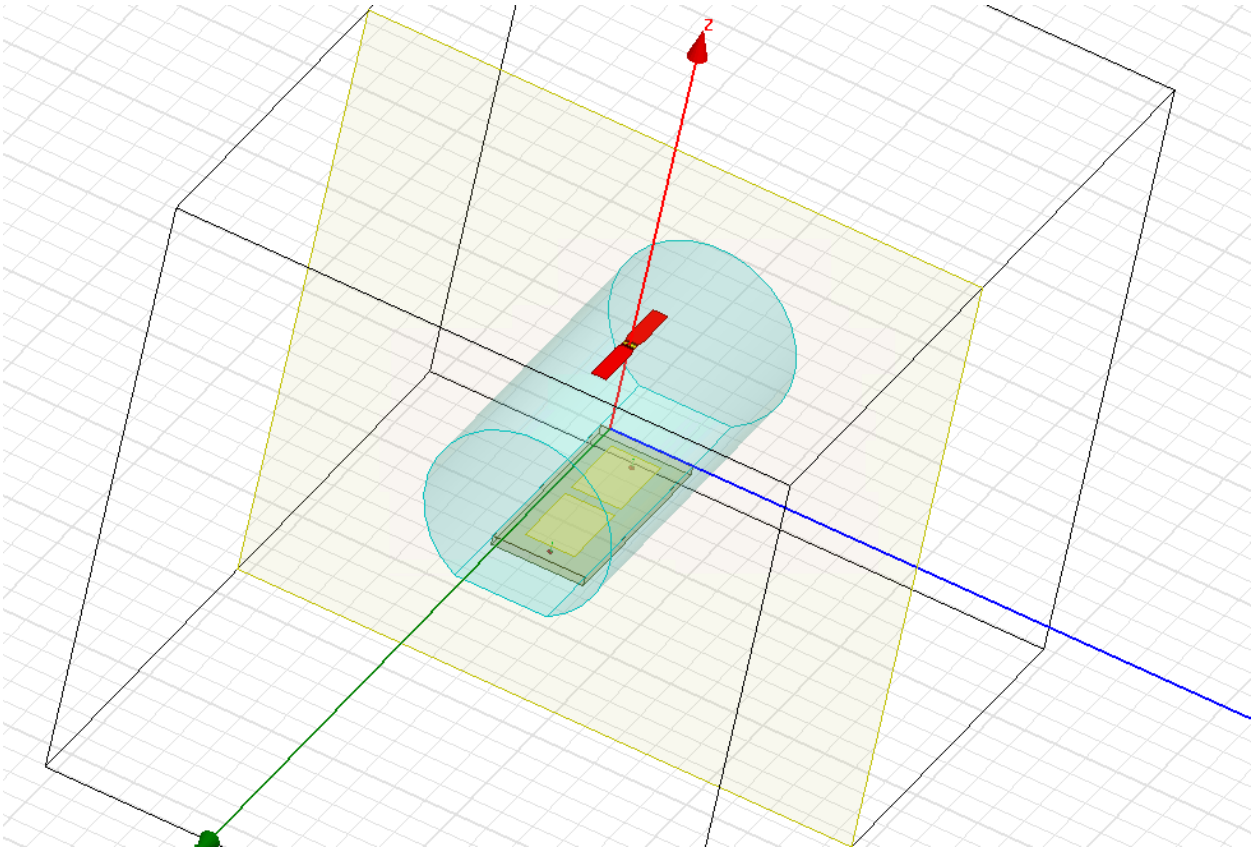

Figure 4.4 Simulation for osteoporosis detection in ANSYS HFSS

4.4 Device description

The developed device is an electromagnetic microwave testbed for highly-sensitive and repeatable measurements of wrist bone signature for osteoporosis detection.

The testbed shown in **Figure 4.5** consists of

[1] Movable top with a 3x1 900 MHz passive RFID antenna array and four pressure sensors (FlexiForce® ESS301);

[2] Fixed bottom with an embedded 2x1 (and replaceable) reader antenna array printed on 128 mil FR4 and a 180° power splitter (ZFSCJ-2-4-S from Mini-Circuits®; two cables from the splitter will be wired together);

[3] Supporting frame, which also measures wrist thickness after applying pressure from top;

[4] A grip (not shown) to fix the arm position.

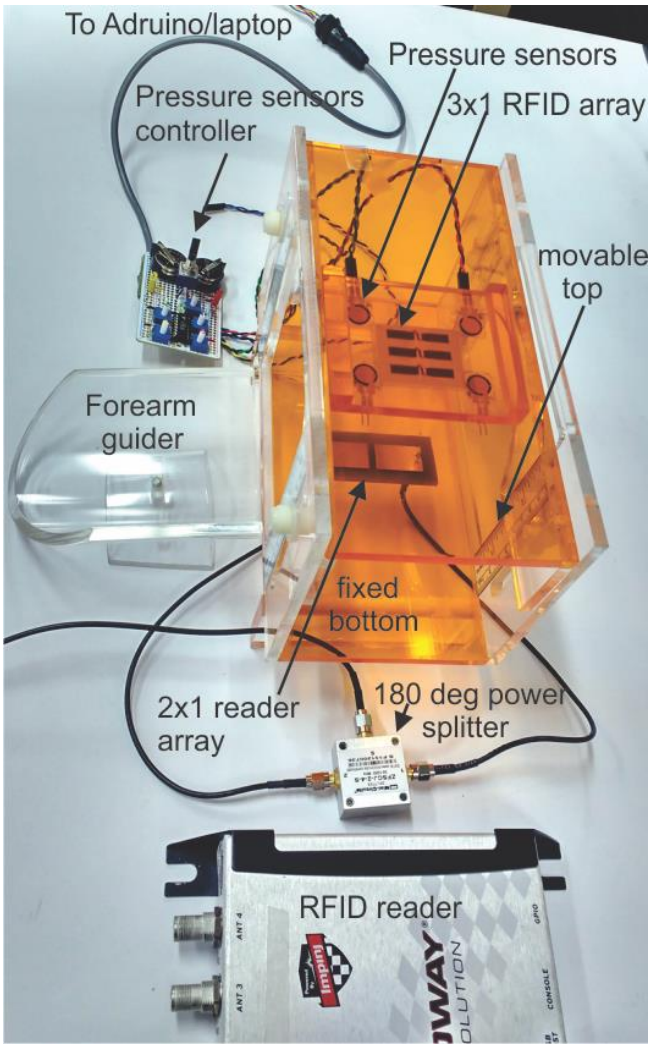

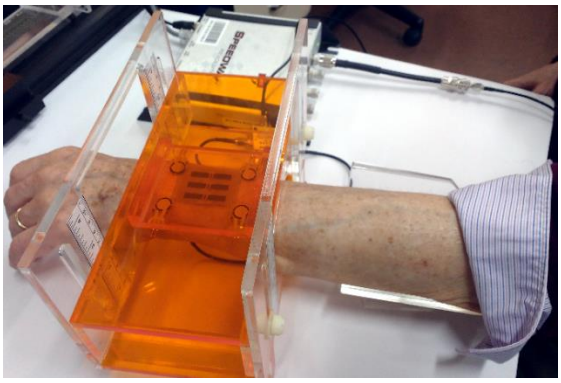

Figure 4.5 Testbed drawing and bone signature measurements.

4.5 Operation concept

A cortical bone shell with trabecular bone matter inside is a scatterer of the electromagnetic signal since the dielectric contrast (ratio of the respective dielectric constants) with the surrounding muscle tissue (or average body tissue) is significant. The dielectric contrast defines the degree of scattering/reflection of an electromagnetic signal at the boundary between two dielectric tissues: the larger the contrast, the stronger the signal loss. In the extreme osteoporotic case, the entire trabecular bone volume is replaced by a mixture of yellow bone marrow and fat, which leads to a much larger average dielectric contrast (about 5-6 vs. 2.8) between the bone and the surrounding tissue. In the general case, measured dielectric constant values for trabecular bone matter with bone loss may vary. On-skin RFID tags should be quite sensitive to this change since the signal travels twice through the bone (from the reader to the tag and vice versa) and gets scattered significantly stronger when the average dielectric contrast increases.

4.6 Key point of the design

The key point of the design is the novel concept of the reader antenna array. Two reader patch antennas form a 2x1 array with two radiators driven out of phase via a 180-degree power splitter. This configuration is known as the Dyson balun. The two antiphase radiators should provide a much greater penetration depth into the body and return signal than one single antenna.

It has been found that the reflection coefficient, S_{11}, of the new reader antenna *alone* (the top RFID array was removed from the frame) reveals a number of resonances. The first two occur at 222±3, 482±3 MHz for five normal volunteers and at 205±2, 470±3 MHz for two volunteers with osteoporosis.

References

[1]. Zhou T, Meaney PM, Pallone MJ, Geimer S, Paulsen KD. Microwave tomographic imaging for osteoporosis screening: a pilot clinical study. Conf Proc IEEE Eng Med Biol Soc. 2010:1218-21. doi: 10.1109/IEMBS.2010.5626442. PubMed PMID: 21096119; PubMed Central PMCID: PMCPMC3752590. Available from: http://www.ncbi.nlm.nih.gov/pubmed/21096119.

[2]. Meaney PM, Goodwin D, Golnabi A, Pallone M, Geimer S, Paulsen KD. 3D Micowave bone imaging. Conf Proc 6th European Conference on Antennas and Propagation (EUCAP) 2011. doi: 10.1109/EuCAP.2012.6206024.

[3]. Golnabi AH, Geimer S, Zhou T, Paulsen KD. Microwave tomography for bone imaging. 2011 IEEE International Sym. on Biomedical Imaging: From Nano to Macro; 2011: 956-959. doi:0.1109/ISBI.2011.5872561.

[4]. Meaney PM, Zhou T, Goodwin D, Golnabi A, Attardo EA, Paulsen KD. Bone dielectric property variation as a function of mineralization at microwave frequencies. Int J Biomed Imaging. 2012:649612. doi: 10.1155/2012/649612. PubMed PMID: 22577365; PubMed Central PMCID: PMCPMC3345233. Available from: http://www.ncbi.nlm.nih.gov/pubmed/22577365.

[5]. Meaney PM, Goodwin D, Golnabi AH , Zhou T, Pallone M, Geimer SD, Burke G, Paulsen KD. Clinical Microwave Tomographic Imaging of the Calcaneus: A First-in-Human Case Study of Two Subjects. IEEE Transactions on Biomedical Engineering. 2012;59(12). doi: 10.1109/TBME.2012.2209202. PubMed Central PMCID: PMC3759252. Availble from http://www.ncbi.nlm.nih.gov/pubmed/22829363

[6]. https://www.radiologyinfo.org/en/info.cfm?pg=osteoporosis

[7]. Image source: http://www.scottsdalesportsmedicine.com/content/dexa-bone-density-scan

Chapter 5

Future Scope and Conclusion

5.1 Future Scope

The ultimate dream is to develop the VHP Family. With the current development in process here are a few proposed ideas for the advancement of CAD phantom research.

5.1.1 Development and Validation of the Full body VHP-Male Model

The VHP dataset has cryosection images available as discusses, using the existing tools for construction of CAD phantoms. Work has begun in this direction [1]. This development is a step closer toward the VHP family. Validating the male model for SAR studies and MRI applications would give us a tool to improve or confirm the existing safety standards.

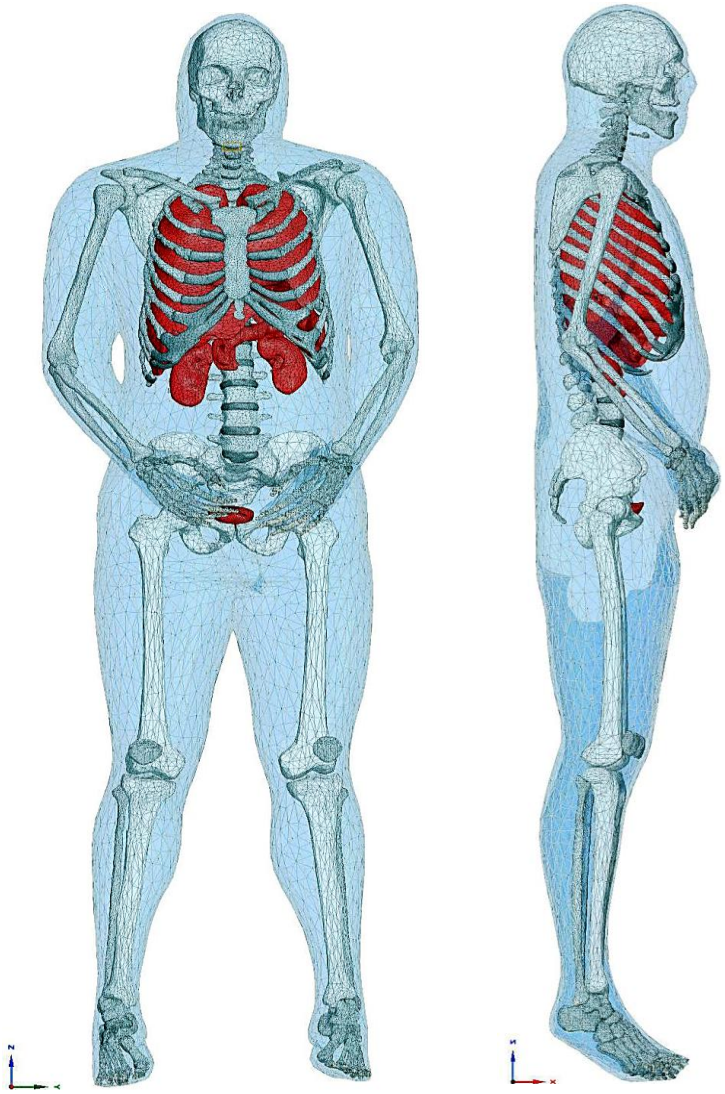

Figure 5.1 VHP-Male Model

5.1.2 Validation of the VHP-Male model

Similar to the VHP-Female model validation, the same test can be applied to the Male model as described in this thesis.

5.1.3 Enhancing the anatomical details

Segmenting new tissues to add to the model which assist in giving enhanced details to the phantom. For example, the latest development is the Ear canal as shown in figure 5.2

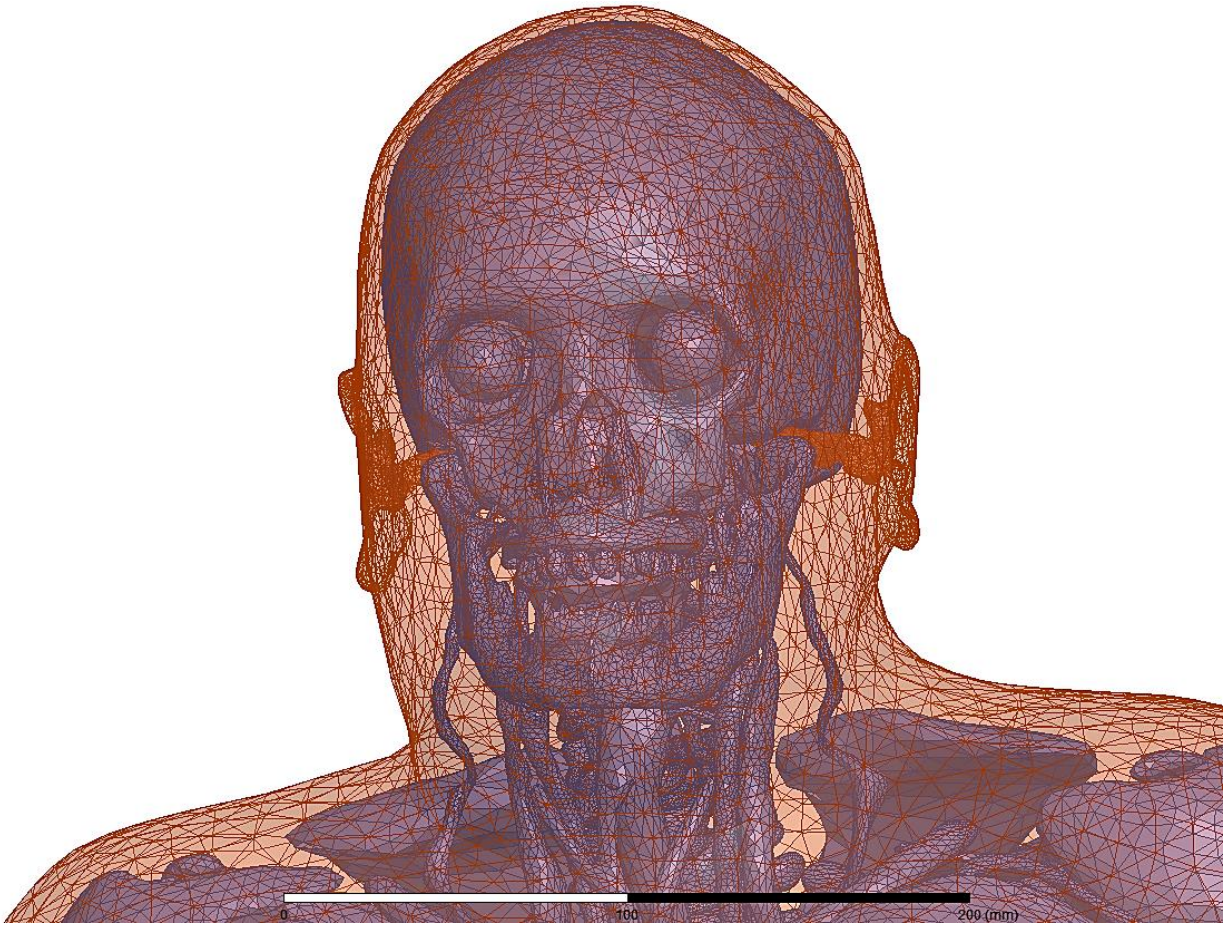

Figure 5.2 VHP- Female v. 4.0, including a highly refined ear canal

5.2 Conclusion

This thesis has presented the recent development in the VHP –Female CAD phantom along with its validation for MRI application. Comparing the simulation results with existing literature enables us to use the VHP-Female v. 3.1 for MRI studies. This serves as a powerful tool for researchers and medical professionals to perform various medical procedures on the phantom instead of human subjects.

The latter part established the novel approach for the detection of osteoporosis. This is still in the development phase and has been tested numerically. The field of CAD Human Phantom is the future for testing experimental medical procedures. This thesis serves as a resource for validating Electromagnetic CAD human phantoms.

References

[1]. P. Lacroix, N. Manino, “Virtual Human Male Model,” Major Qualifying Project, Dept. Elect. and Computer Eng., Worcester Poly. Inst., April 2017.

Appendix A

Computing sources (or excitations) for the perfectly-tuned “universal” coil model based on the port data obtained from CEM simulations – a MATLAB script

```
%   Eigenmode method for constructing the "universal" coil
%   NEVA Electromagnetcs, LLC Sep. 2016
clear all

%%  Import port matrices
Z_matrix;
S_matrix;
Z = squeeze(Z);
S = squeeze(S);
N_rungs = size(Z,1)/2;

%%  Construct eigenvectors/eigenvalues of the Z-matrix
Z = -Z;          %  negative impedance matrix
[I, D] = eig(Z); %  compute eigenmodes
lambda = diag(D);
C0 = real(1./(1j*(2*pi*f)*lambda));    %terminating capacitances for each
mode

keep = C0 > 0; % filter out negative capacitances
C0 = C0(keep);
I = I(:,keep);

%%  Find mode signature and select the dominant resonant modes
mode_signature = exp(2j*pi*(0:N_rungs-1)/N_rungs); % sinusoidal mode
signature
mode_strength = abs(mode_signature * I(1:N_rungs,:));
[~, ind] = sort(mode_strength, 'descend'); % keep the two modes with the
largest mode strength
C0 = C0(ind(1:2));
I = I(:,ind(1:2));
C0_pF = C0 * 1e12

%%  Find excitation sources
Z0_S = 50;
V = Z * I;          %   voltages for the coil ports
A = V + Z0_S * I;   %   incident normalized power waves
B = S * A;          %   reflected normalized power waves
P_raw = 0.5 * (sum(abs(A).^2) - sum(abs(B).^2)); % power dissipated in the
coil
A(:,1) = A(:,1) / sqrt(2 * P_raw(1)); % normalize coil drive power to 1W
(0.5W per mode)
A(:,2) = A(:,2) / sqrt(2 * P_raw(2));
```

```
sources =  A * [1, 1; 1j, -1j]; % combine modes to create circular
polarization
mode_strength = abs(mode_signature * sources(1:N_rungs,:));
[~, ind] = sort(mode_strength); % sort sources by circular polarization
direction
sources = sources(:, ind);

%%  Output excitation sources in EXCEL format
f = fopen('sources1_eigZ.csv','wt');
fprintf(f, 'Source,Magnitude,Phase');
for i=1:size(sources,1)
    fprintf(f, '\n%u:1,%.8gW,%.8gdeg', i, 0.5 * abs(sources(i,1)).^2,
angle(sources(i,1)) * 180 / pi);
end
fclose(f);
f = fopen('sources2_eigZ.csv','wt');
fprintf(f, 'Source,Magnitude,Phase');
for i=1:size(sources,1)
    fprintf(f, '\n%u:1,%.8gW,%.8gdeg', i, 0.5 * abs(sources(i,2)).^2,
angle(sources(i,2)) * 180 / pi);
end
fclose(f);
```